Correspondence to:
L. M. Pichel,
leonardo.munizpichel@manchester.ac.uk

The Impact of Pre-Salt Rift Topography on Salt Tectonics: A Discrete-Element Modeling Approach

Leonardo M. Pichel[1,2,3] ID, **Emma Finch[1]** ID, and **Rob L. Gawthorpe[2]** ID

[1]School of Earth and Environmental Sciences, University of Manchester, Manchester, [2]Department of Earth Science, University of Bergen, Bergen, Norway, [3]Now at Basins Research Group (BRG), Department of Earth Science and Engineering, Imperial College, London, UK

Abstract Gravity-driven salt tectonics along passive margins is commonly depicted as comprising domains of updip extension and downdip contraction linked by an intermediate, broadly undeformed zone of translation. This study expands on recently published physical models using discrete-element modeling to demonstrate how salt-related translation over pre-salt rift structures produce complex deformation and distribution of structural styles in translational salt provinces. Rift geometries defined by horsts and tilted fault-blocks generate base-salt relief affecting salt flow, diapirism and overburden deformation. Models show how flow across pairs of tilted fault-blocks and variably-dipping base-salt ramps associated with pre-salt faults and footwalls produce abrupt flux variations that result in alternation of contractional and extensional domains. Translation over tilted fault-blocks defined by basinward-dipping normal faults results in wide, low amplitude inflation zones above footwalls and abrupt subsidence over steep fault-scarps, with reactive diapirs that are squeezed and extrude salt as they move over the fault. Translation over tilted-blocks defined by landward-dipping faults produces narrow inflation zones over steep fault-scarps and overall greater contraction and less diapirism. As salt and cover move downdip, structures translate over different structural domains, being inverted and/or growing asymmetrically. Our models allow, for the first time, a detailed evolution of these systems in cross-section and demonstrate the effects of variable pre-salt relief, salt sub-basin connectivity, width and slope of base-salt ramps. Results are applicable to syn- and post-rift salt basins; ultimately improving understanding of the effects of base-salt relief on salt tectonics and working as a guide for interpretation of complex salt deformation.

1. Introduction

Gravity-driven salt-related deformation on passive margins is commonly depicted as kinematically-linked domains of updip extension and downdip contraction with an intermediate, broadly undeformed zone of translation (Figure 1a) (Brun & Fort, 2011; Hudec & Jackson, 2004, 2007; Jackson, Jackson, Hudec, & Rodriguez, 2015; Quirk et al., 2012; Rowan et al., 2000, 2004). More recent studies (Dooley et al., 2017; Dooley & Hudec, 2017; Pichel et al., 2018) have shown that this structural zonation represents a simplified view of regional salt tectonics and other factors exert a significant effect on the variability of structures developed in space and time. Salt behaves as a viscous fluid over typical geological strain-rates (e.g. Gemmer et al., 2004; Jackson & Hudec, 2017), and is, therefore, sensitive to the geometry of the surface it flows across (Dooley et al., 2017, 2018; Pichel et al., 2018). As a result, a significant factor influencing the development of salt structures is pre-salt topography (Figure 1b) (Dooley et al., 2017; 2018; Pichel et al., 2018).

Late syn-rift to early post-rift salt basins commonly possess variable salt thickness across base-salt relief as salt is deposited over a topography inherited from a previous rift phase (post-rift salt) or formed during salt deposition (syn-rift salt). In most cases, salt basins are hybrid, with salt being post-rift landward and syn-rift basinward as rifting propagates towards the embryonic oceanic spreading centre, such as in the South and Central Atlantic basins (Rowan, 2014; Rowan, 2018; Tari et al., 2017). Examples of early post-rift salt basins with significant pre-salt relief include the hydrocarbon-prolific Gulf of Mexico (Dooley & Hudec, 2017; Hudec et al., 2013; Peel, 1995; Rowan et al., 2004) and South Atlantic basins (Davison et al., 2012; Hudec & Jackson, 2004; Jackson et al., 2008; Jackson, Jackson, & Hudec, 2015; Jackson, Jackson, Hudec, & Rodriguez, 2015; Mohriak et al., 1995; Quirk et al., 2012). Late syn-rift salt basins, however, e.g., Nova Scotia (Albertz et al., 2010; Deptuck & Kendell, 2017; Ings & Shimeld, 2006), Morocco and Mauritania (Tari et al., 2000, 2003, 2017; Tari & Jabour, 2013) are associated with more extreme variations of initial
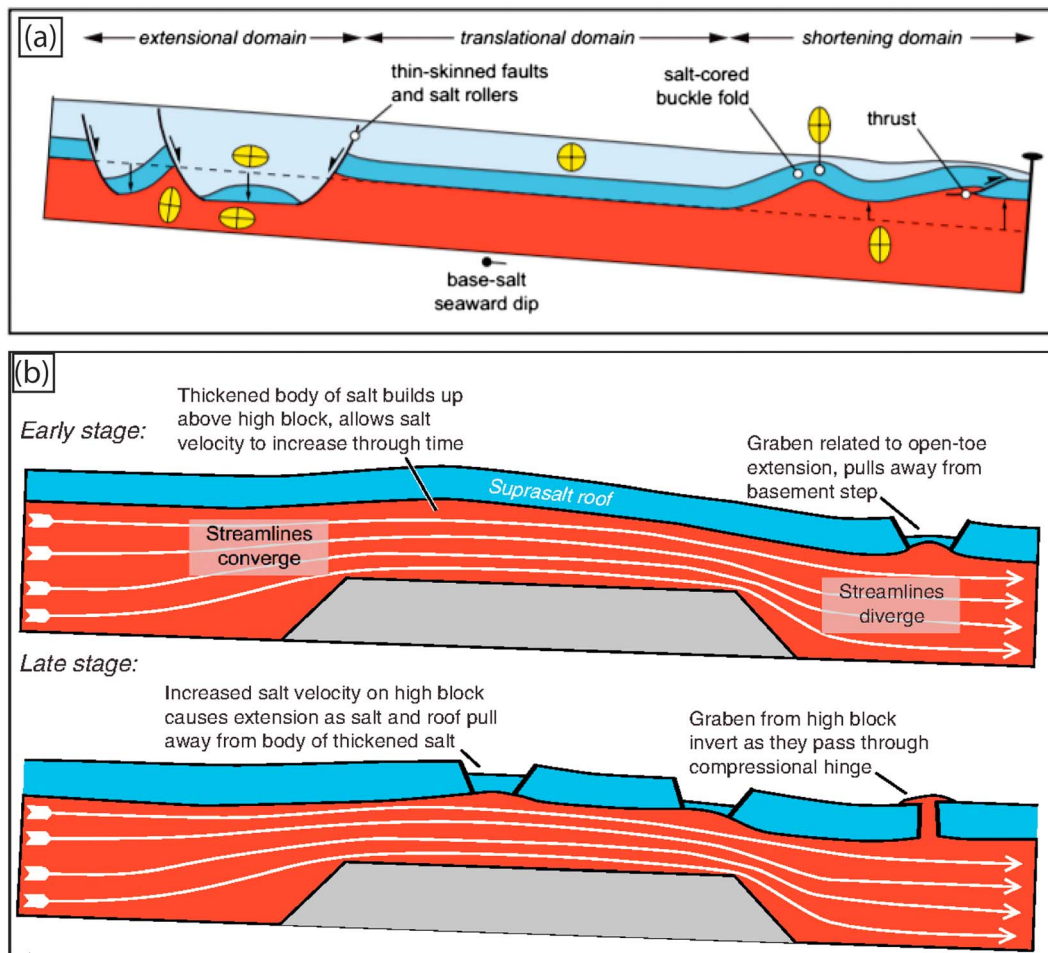
Figure 1. (a) Classical distribution of regional salt tectonics structural domains in passive margins: Updip extensional and downdip contractional domains kinematically linked by an undeformed translational province (from Jackson, Jackson, Hudec, & Rodriguez, 2015). (b) Kinematic model based on recent physical models showing effects of salt-related translation across pre-salt topography and consequent variations of salt flux (streamlines) resulting in complex deformation history and localized zones of deformation. These are characterized by salt inflation followed by extensional collapse over the updip edge of the horst; and a monoclinal zone of subsidence limited by updip extension and downdip contraction over its downdip edge (from Dooley et al., 2017).

salt thickness both within and across grabens (Jackson & Hudec, 2017). Where basement fault throw is larger than salt thickness, salt basins are separated into sub-basins that evolve independently (Jackson & Hudec, 2017). In intermediate scenarios (i.e. late syn- and early post-rift salt), lateral flow between sub-basins occurs but pre-salt topography disrupts and limits downdip translation (Jackson & Hudec, 2017).

Early physical models simulated progradation over stepped (Ge et al., 1997) and syn-rift salt basins (Adam & Krézsek, 2012), providing important insight into the effects of differential loading and their structural evolution. These studies, however, did not address the significant effects of early gliding and downdip translation associated with post-rift thermal subsidence and basinward tilting typical of passive margins (Jackson, Jackson, Hudec, & Rodriguez, 2015; Peel, 2014; Rowan et al., 2004). Recent analogue models (Dooley & Hudec, 2017; Dooley et al., 2017, 2018) have demonstrated how translation across pre-salt relief promotes salt flux variations that result in complex, multiphase salt tectonics and localized zones of deformation (Figure 1b). These pioneering studies focused on the plan-view evolution and final cross-sectional variations of these systems, not analyzing their cross-sectional sequential evolution and variations in diapirism style (i.e. reactive, passive and active, Hudec & Jackson, 2007; Vendeville & Jackson, 1992) relative to changes in salt flow and overburden deformation patterns.

In this study, we employ a Discrete-Element Modeling (DEM) approach (Abe & Urai, 2012; Finch et al., 2003, 2004; Pichel et al., 2017; Schöpfer et al., 2006) to investigate translation across semi-isolated salt sub-

basins. These sub-basins are associated with horst and tilted fault-blocks that are realistic base-salt geometries along rifted passive margins. This approach allows for analysis of how salt flux and overburden deformation are affected by: 1) the presence of two pre-salt structures (i.e. tilted fault-blocks), 2) base-salt ramps with different slopes and dip-direction according to the geometry of the underlying pre-salt structures, and 3) variable base-salt step height and connectivity between salt sub-basins. These results are important for understanding the complexity and evolution of salt-related deformation and to guide interpretation of complex salt and supra-salt structures along rifted passive margins and intracratonic salt basins. Furthermore, our results show that salt and supra-salt geometries can be directly linked to pre-salt structures and, therefore, recognition of similar structural patterns on continental margins can aid in the identification of (usually) poorly-imaged pre-salt structures.

2. Method and Models Design

While physical models provide invaluable insight into the 3D geometry, timing and planform sequential evolution of structures (Dooley et al., 2007, 2015; Ferrer et al., 2012, 2017; Vendeville and Jackson, 1992; 1995), they demand a significant amount of time, space and investment (Pichel et al., 2017). Numerical models based on continuum methods, such as finite-element modeling (FEM), have proved very useful in understanding the dynamics of salt flow, allowing more numerical control and realistic stress–strain quantification (Albertz et al., 2010; Gemmer et al., 2004; Gradmann et al., 2009; Weijermars et al., 2015). They are not able, however, to reproduce spontaneous, realistic fault localization and propagation in the cover, which is critical to understand the kinematic and structural style of minibasins and diapirs in areas affected by regional stresses. Thus, FEM cannot reproduce accurately the development of reactive diapirs driven by regional extension (Vendeville & Jackson, 1992), which are important for the focus of this study.

As with any other modeling technique, Discrete-Element Modeling (DEM) has advantages and disadvantages (as discussed in Botter et al., 2014). DEM limitations regard the need of meticulous calibration of particle parameters (Botter et al., 2014) and, because of its discontinuous nature, the (Newtonian) viscous behaviour of salt is approximated (Abe & Urai, 2012; Pichel et al., 2017). Nevertheless, the method allows a good first-order approximation of viscous salt flow at a regional scale that can be used to analyze various aspects of salt tectonics and diapirism driven by regional stresses (Pichel et al., 2017). The advantages of DEM are: 1) scaling is not a restriction; 2) models are easily reproducible, not requiring constant and complex re-meshing; 3) they provide higher resolution and analysis of small-scale deformation within the overburden; and, 4) they promote a more realistic, natural development and evolution of faults and folds in the sedimentary cover than other numerical techniques (Finch et al., 2003, 2004; Pichel et al., 2017). The DEM technique used in this study derives from the Lattice Solid Model (Mora & Place, 1993, 1994; Place et al., 2002) and the Particle Dynamics Method (Finch et al., 2003). The technique has been extensively applied to model the dynamic evolution of geological systems (Donzé et al., 1994; Place et al., 2002), including faulting and folding processes (Deng et al., 2017; Finch et al., 2003, 2004; Finch & Gawthorpe, 2017; Schöpfer et al., 2006); and viscous flow associated with development of boudinage structures (Abe & Urai, 2012) and salt diapirism (Pichel et al., 2017).

The rock mass is treated as an assemblage of circular elements linked by breakable elastic springs through a 'repulsive-attractive' force obeying Newton's Laws of motion (Finch et al., 2004; Hardy & Finch, 2006; Mora & Place, 1993, 1994). The relative strength of each assemblage is defined by its breaking separation, so particles remain bonded until this threshold is exceeded (Donzé et al., 1994; Finch et al., 2004). The motion of particles is assumed to be frictionless and cohesionless with elasto-plastic and ductile behaviour for the overburden and salt, respectively (Finch et al., 2003; Hardy & Finch, 2007; Pichel et al., 2017). The elements have four radii of 0.2, 0.3, 0.4 and 0.5 units and are randomly distributed to reduce failure in preferential orientations within the matrix. A viscous term (v) is added to counteract the elastic behaviour and buildup of kinetic energy within a closed system, enabling its stabilization, which makes it ideal for studying quasi-steady tectonic processes (Finch et al., 2004; Pichel et al., 2017).

Forces are resolved in the x and y directions and elements are also subjected to gravitational forces, F_g. The equations that define the inter-relationship of all forces acting on the DEM are:

$$F_x = F_{i,n} - v\dot{x} \tag{1}$$

$$F_y = F_{i,n} - v\dot{y} + F_g \tag{2}$$

Where $F_{i,n}$ corresponds to the total elastic force acting on a particle, v represents the dynamic viscosity and and correspond to the velocity of the particle.

In order to make DEM applicable to regional-scale salt tectonics, the properties of elements representing salt are adjusted so they behave macroscopically as a viscous-plastic material. This is achieved by assigning them a negligible breaking separation so their motion is entirely controlled by the viscosity and gravity of the system (Pichel et al., 2017). This does not reproduce the entire range of salt-related mechanical processes; but, based on stress–strain responses obtained by compressional tests (Pichel et al., 2017, Figure 2), works as a good first-order approximation for regional studies. These tests show that a separation threshold of 0.001 of particles assigned to salt produces a linear, horizontal response with negligible elastic component. This response is representative of ductile viscous-plastic materials, and notably similar to curves produced by physical (Spiers et al., 1990) and numerical (Li & Urai, 2016) experiments of salt deformation.

The model salt viscosity is 1.1 x10^9 Pa.s, which is lower than its real viscosity (10^{17}–10^{20} Pa s – Gemmer et al., 2004; Jackson & Hudec, 2017). However, as models of salt flow involve solid-state creep, negligible inertial forces and Reynolds number (Re < <1), geometric similarity ensures dynamic and kinematic similarity despite numerical parameters not being identical to the real world (Pichel et al., 2017; Schultz-Ela et al., 1993; Weijermars et al., 1993; Weijermars & Schmeling, 1986). The Poisson's ratio (v) for 2D DEM models is 0.33 and the Young Modulus (E) of the elasto-plastic overburden is of 6.75 GPa. These values are similar to previous studies of salt tectonics (Pichel et al., 2017), and in the range of natural examples of salt and an overburden composed of semi-consolidated siliciclastic rocks or marls (Johnson & DeGraff, 1988; Liang et al., 2007). For a full and more detailed description of scaling of parameters and equations governing DEM, the reader is referred to Mora and Place (1994), Finch et al. (2004); Hardy and Finch (2005, 2006) and Pichel et al. (2017).

We present three models where the impact of typical pre-salt rift structures on early-stage salt tectonics, i.e. gliding over a regionally dipping salt detachment (Rowan et al., 2004; Peel, 2014), is tested: i) Model A: horst (Figure 2a), ii) Model B: tilted fault-blocks with basinward-dipping normal faults (Figure 2b), and iii) Model C: tilted fault-blocks with landward-dipping normal faults (Figure 2c). Salt-related gliding and viscous shear drag within the salt are associated with the process of post-rift thermal subsidence and associated margin tilt (e.g. Peel, 2014; Pichel et al., 2018; Rowan et al., 2004). These processes are reproduced in the models by simulating salt-related translation over a 3° basinward-dipping salt detachment (Figure 2), which is in agreement with the slope of salt detachment on passive margins (Peel, 2014; Tari et al., 2003) and previous models (Brun & Fort, 2011; Dooley et al., 2007; Dooley et al., 2015, 2017; Pichel et al., 2017).

The horst model (A) presents a setting similar to that modeled in Dooley et al. (2017) to illustrate how the approach reproduces the expected kinematics and strain-distribution associated with salt-related translation across pre-salt relief. In addition, we evaluate the sequential evolution of structures in cross-section, something not analyzed by Dooley et al. (2017). The model comprises a single central horst (8 km wide and 1.35 km high) defined by a landward- and a basinward-dipping (50°) normal fault at its updip and downdip edges, respectively (Figure 2a). The tilted fault-block models (B and C) display novel scenarios where we evaluate the influence of steep and gentle base-salt ramps associated with syn-rift normal faults and their footwalls respectively (Figure 2b-c). These models comprise a pair of equidimensional, 10 km wide asymmetric fault-blocks with a 50°-dipping normal fault and a gentle (7.5°) footwall with 1.35 km of maximum structural relief at its crest (Figure 2b-c, Table 1). In an additional set of experiments, we evaluate the effects of variable structural relief and connectivity between salt sub-basins by varying the central footwall crest height (Models B1-B4 and C1-C4, Figure 2d-e) (Table 1), while maintaining its location relative to model boundaries.

Particles within the salt and overburden are subject to gravitational settling in order to ensure mechanical stability, producing an initial subtle monoclinal relief at the edges of pre-salt structures (Figure 2). This is caused by preferential flow within the salt driven by the basinward dip of the model immediately prior to overburden translation. The monocline and cover outer-arc extension are also typical geometries associated
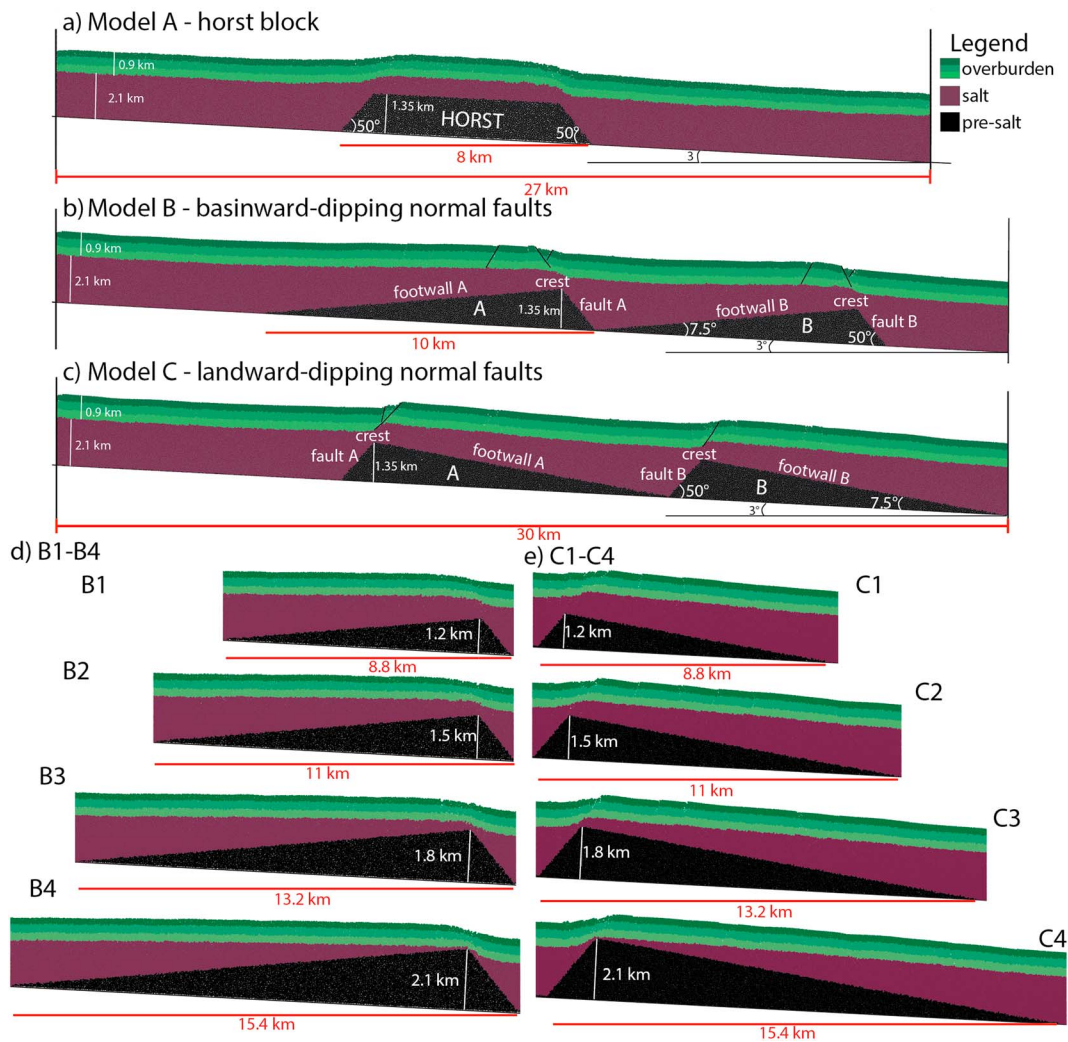
Figure 2. Initial model designs, dimensions and thicknesses after a phase of particle settling for the main experiments presented in this study: (a) Model A: Horst; (b) Model B: Basinward-dipping normal faults; (c) Model C: Landward-dipping normal faults; (d) Focused views showing variation of structural relief and salt connectivity for basinward-dipping normal faults (models B1-B4); and (e) for landward-dipping normal faults (models C1-C4). The modeled media consists of a box with free walls and rigid, undeformable pre-salt structures (black). The models have an initial thickness of 3 km, with the salt section (magenta) having a maximum thickness of 2.1 km and minimum thickness over the footwall crest decreasing as the structural relief increases for models B1-B4 and C1-C4, with no salt over the footwall crest of models B4 and C4. The pre-kinematic overburden (green) has constant thickness of 900 m.

Table 1
Summary of variable input parameters for all models

	Pre-salt faults dip-direction	Block length (km)	Step height (km)	Min salt thickness (km)
Model A	Land- and basinward	8	1.35	0.75
Model B	Basinward	10	1.35	0.75
Model C	Landward	10	1.35	0.75
Model B1	Basinward	8.8	1.2	0.9
Model B2	Basinward	11	1.5	0.6
Model B3	Basinward	13.2	1.8	0.3
Model B4	Basinward	15.4	2.1	0
Model C1	Landward	8.8	1.2	0.9
Model C2	Landward	11	1.5	0.6
Model C3	Landward	13.2	1.8	0.3
Model C4	Landward	15.4	2.1	0

with end of rift stretching and syn-depositional salt flow (Duffy et al., 2013; Jackson & Hudec, 2017; Rowan, 2014). For simplicity and general applicability, we do not simulate syn-kinematic sedimentation and assume a homogeneous overburden underlain by a salt interval with densities of, respectively, 2.3 g cm^{-3} and 2.16 g cm^{-3}. These values concur with nature and previous physical and numerical analogues (Albertz & Ings, 2012; Dooley et al., 2009, 2012; Gemmer et al., 2005; Gradmann & Beaumont, 2016; Ings & Shimeld, 2006). The maximum and minimum salt thicknesses for each model are 2.1 km and 750 m respectively, due to gradual thinning of the salt across pre-salt structural highs. The pre-kinematic overburden has a constant thickness of 0.9 km. As both thickness and density ratios of models and natural examples are similar, stresses in the overburden are dynamically scaled (Pichel et al., 2017; Weijermars et al., 1993). Models are run for 5 million time-steps, which are scaled to 10 Ma in order to simulate translation rates and magnitudes compatible to the early-stage salt-related deformation typical of passive margins (Jackson and Hudec, 2005; Peel, 2014; Pichel et al., 2018; Rowan et al., 2004). Thus, a total of 7.5 km of downdip translation is produced by moving model end-walls basinward at an equal and constant rate of 0.75 mm/year, equivalent to a strain-rate in the order of 10^{-16} s^{-1}, within the typical range of salt tectonics along passive margins (Jackson & Hudec, 2017; Pichel et al., 2018; Rowan et al., 2004). The boundaries of the models are not shown because these are not relevant in this study, which focuses on deformation above pre-salt rift structures.

3. Salt Flow Across a Horst (Model A)

Model A shows that as the salt and overburden move downdip across a pre-salt horst, salt flux variations occur at its edges generating localized zones of deformation that expand through time (Figure 3). Flux mismatches occur in response to local changes in the cross-sectional area of flow as the entire system moves across the pre-salt rift topography and the associated base-salt ramps. A salt surplus and inflation occur over the landward-dipping normal fault defining the updip edge of the horst; whereas salt deficit and thinning take place over the downdip, basinward-dipping normal fault (Figure 1b) (c.f. Dooley et al., 2017; 2018). As the salt is originally thicker updip of the horst, the amount of salt being fed towards its updip edge is higher than the amount of salt leaving it, resulting in salt inflation and contraction. Conversely, the amount of salt moving across the downdip edge is significantly less than the amount moving away, producing salt deficit and a monoclinal zone of subsidence that is limited by an extensional hinge at the top of, and a contractional hinge at the base of, the basinward-dipping normal fault (Figure 3) (c.f. Dooley et al., 2017; 2018).

During the first 4 Myr, minor salt inflation and cover uplift occur over the updip edge of the horst (Figure 3a-b). As translation continues and salt gradually thickens, it begins to accelerate and extend as it moves over the gentle and wide basinward-dipping crest of the horst (Figure 3b). Over its downdip edge, a monoclinal zone of subsidence develops, being defined by extension above the top of, and contraction above the base of, the pre-salt basinward-dipping normal fault. The extensional zone is characterized by reactive diapirism and predominantly basinward-dipping listric normal faults in the cover with salt rollers in their footwalls (Figure 3a-b). The contractional zone is defined by basinward-verging thrusts, salt inflation, cover uplift and folding with outer-arc extension (Figure 3a-b). During the first 2 Myr, a symmetric reactive diapir (1_R, Figure 3a) forms at the top of the basinward-dipping pre-salt fault where extension is greater (Figure 3a). In the next 2 Myr, new reactive diapirs (2_R and 3_R, Figure 3b) form at this point as the earlier one (1_R, Figure 3b) moves downdip. During this stage (at 4 Myr), an imbrication of thrusts starts to impose differential structural loading driving additional salt attenuation at the base of the pre-salt fault and inflation further downdip (Figure 3b).

With continued downdip translation, salt flux variations are amplified, increasing updip salt inflation and cover uplift, and downdip salt depletion and cover subsidence (Figure 3c). A broad salt anticline forms over the updip, landward-dipping fault, whereas over the basinward-dipping fault, deformation becomes progressively more complex and inversion of previous structures occurs (Figure 3b-c). New reactive diapirs (4_R and 5_R, Figure 3c) originate at the top of the basinward-dipping fault (i.e. base-salt extensional hinge). Immediately downdip, extensional structures that originally formed near the top of the fault move across a contractional hinge at its base and are inverted (Figure 3a-c). Normal faults are reactivated as thrusts with minor salt flow in their hangingwall and reactive diapirs (1_R and 2_R, Figure 3b) are squeezed (1_S and 2_S, Figure 3c).
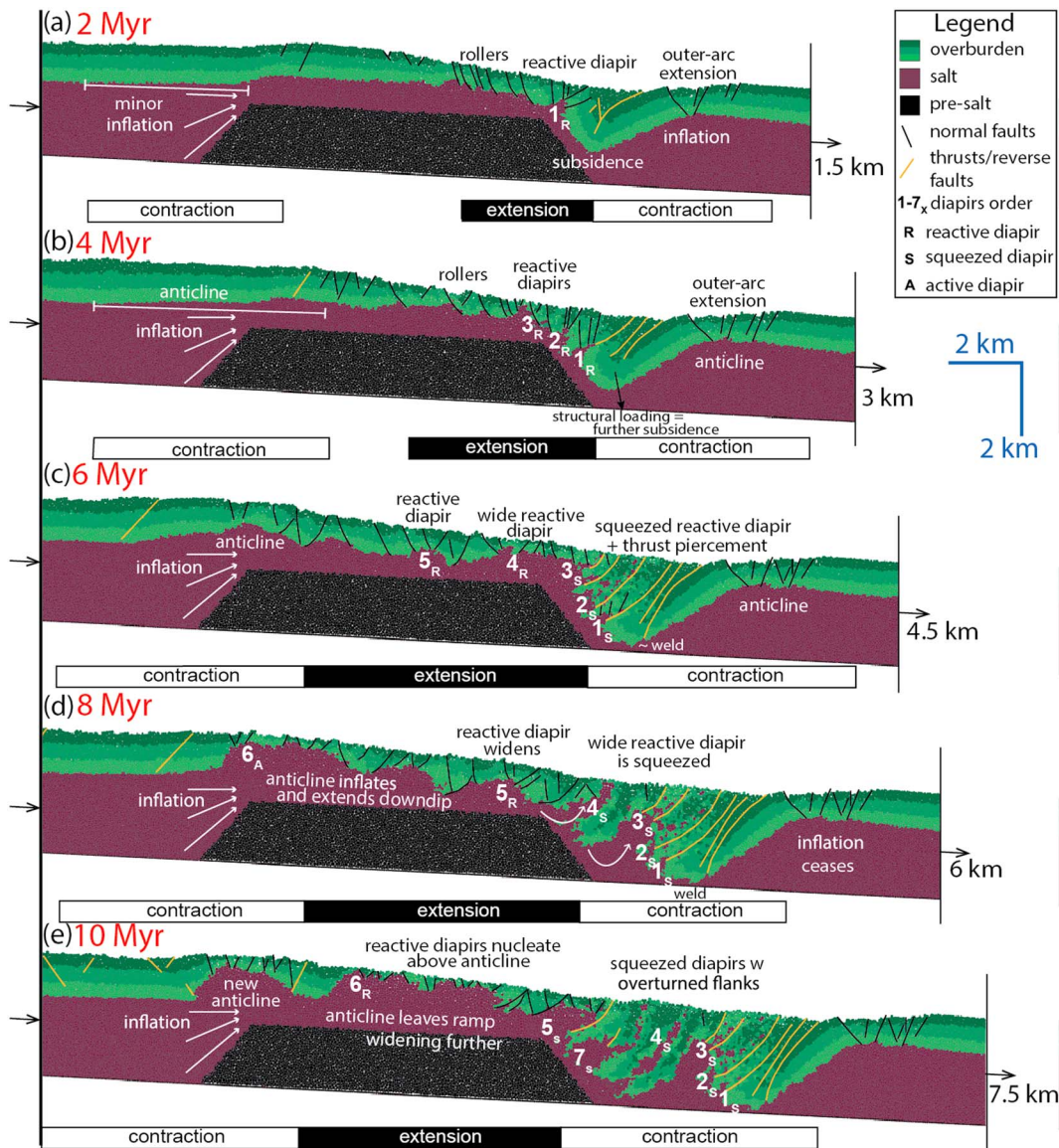
Figure 3. (a-e) Sequential evolution shown in increments of 2 Myr of Model A: Horst, which simulates translation over a single pre-salt horst and consequent salt flux variations across a simple base-salt topography. Model edges are not shown to improve visualization of relevant structures at the centre of the model. As the system translates, structures move over different structural domains, being reactivated and/or inverted. These extensional (black box) and contractional (white boxes) domains shift over time. Diapirs are represented by numbers 1–7 and their corresponding style of growth is indicated in subscript.

At 8 Myr, continuous inflation over the landward-dipping fault promoted thickening and widening of the salt anticline, which moves partially over the basinward-dipping crest of the horst (Figure 3d). As a consequence, the anticline undergoes asymmetric, hybrid growth characterized by an active diapir that uplifts and pierces the overburden on the updip limb of the anticline (6_A, Figure 3d); while its downdip limb extends as it glides over the crest of the horst. At the downdip edge of the horst, the wide reactive diapir (4_R, Figure 3d) moves across the basinward-dipping fault, being squeezed and rising further above the contractional hinge (4_S, Figure 3d). Continuous salt depletion over this fault reduces lateral flow and, consequently, a primary weld forms downdip of the horst causing contraction to migrate landward over the pre-salt fault (Figure 3d).

By the end of the model, the broad anticline that initially formed over the landward-dipping fault has translated completely over the crest of the horst (Figure 3e). This inflated salt body undergoes further extension, being pierced by small reactive diapirs while a new, smaller anticline forms updip, over the landward-

dipping fault (Figure 3e). These geometries and kinematics are similar to the patterns observed in physical models (Figure 1b) (Dooley et al., 2017). Over the basinward-dipping fault, as salt is dramatically thinned between diapirs (4_S and 7_S, Figure 3e), the two salt sub-basins defined by the horst become partially disconnected. As a consequence, the reactive diapir (5_R, Figure 3d) formed at the top of the fault is squeezed (5_S, Figure 3e) over the earlier formed diapirs resulting in a set of basinward-leaning squeezed diapirs with overturned flanks and, occasionally, secondary welds (2-4_S and 7_S, Figure 3e).

4. Pre-Salt Tilted Fault-Blocks With Basinward-Dipping Normal Faults (Model B)

This model simulates a more complex scenario where salt and overburden translation is affected by a pair of tilted pre-salt fault-blocks (A and B), defining gentle landward-dipping (Footwalls A and B) and steep basinward-dipping base-salt ramps (faults A and B, Figure 2b and 4). Similar to Model A, due to cross-sectional variations of salt flux across base-salt relief, salt inflation and contraction occur above the landward-dipping base-salt ramp, and a monoclinal zone of subsidence and salt depletion limited by extensional and contractional hinges develop over the basinward-dipping base-salt ramp (Figure 4). However, because of the variable width and dip of these base-salt ramps and their connection with another set of similar structures downdip, flux mismatches and the complexity of deformation are greater.

During the first 2 Myr, mild inflation and overburden uplift occurs at the updip edge of Fault-block A (Figure 4a). The effect is less evident over Fault-block B because basinward movement of the system is partially obstructed by Fault-block A, although deformation above and downdip of Fault B is greater due to an unimpeded basinward advance beyond the fault. There, a 3 km wide zone of extension and reactive diapirism (1_R, Figure 4a) develops over the crest of Fault B, passing into salt thinning and cover subsidence above the fault, and inflation further downdip. From 2 to 4 Myr (Figure 4b), the inflation zone over Footwall A widens and subsidence over Fault B increases. The earlier-formed reactive diapir (1_R, Fault-block B) rises further due to increased extension, and new extensional faults and a reactive diapir (2_R, Figure 4b) form immediately updip. In contrast, earlier-formed normal faults are inverted as they move across Fault B (Figure 4a-b).

From 4 to 6 Myr, the inflation/contraction zone associated with Footwall A widens and salt flux variations become greater over Fault A and Footwall B (Figure 4c). This results in mild subsidence over Fault A with normal faulting at its crest and reverse faults over its base and into Footwall B (Figure 4c). The first reactive diapir (1_R, Figure 4a-b) emerges and starts to grow passively as it is further extended by moving over the extensional hinge at the crest of Fault B (1_P, Figure 4c). At the same time, salt continues to thin over Fault B while new thrusts form immediately downdip at its base, where salt flow decelerates (Figure 4c). By 8 Myr (Figure 4d), continuous inflation and contraction along Footwall A resulted in the development of two salt anticlines, whereas subsidence and the associated updip extension and downdip contraction are amplified above Fault A. Normal faulting and reactive diapirism occur at the extensional hinge over the crest of the fault, whereas reverse faulting and active diapirism take place at the contractional hinge over the base of the fault, with salt inflation further downdip over Footwall B (Figure 4d). Over Fault-block B, a wide reactive diapir (3_R, Figure 4d) nucleated at the edge of the previously inflated salt body as it extensionally collapsed when it reached the extensional hinge at the footwall crest of Fault B. The earlier-formed passive and reactive diapirs (1_P and 2_R, respectively, Figure 4c) moved across this fault and were squeezed and rotated basinward (1-2_S, Figure 4d). The initial diapir (1_S, Figure 4d) became almost completely pinched-off with salt extruding from its crest to produce a small salt sheet (Sh_1, Figure 4d).

This abrupt alternation of structural styles led to the development of a hybrid diapir above Fault A (4_H, Figure 4d). The diapir (4_H, Figure 4d) is triangular in shape, being characterized by inward-dipping and younging normal faults and a sub-regional and sub-horizontal extended roof on its updip flank, a geometry characteristic of reactive diapirs formed by extension (*sensu* Vendeville & Jackson, 1992). Its downdip flank, however, presents a typical upturned and uplifted flap geometry denoting active rise (c.f. Hudec & Jackson, 2007; Schultz-Ela et al., 1993). This indicates that the diapir rose by extension on its updip flank located over the crest of Fault A (e.g. extensional hinge); and by contraction, upturning its downdip flank over the base of the fault (e.g. contractional hinge).
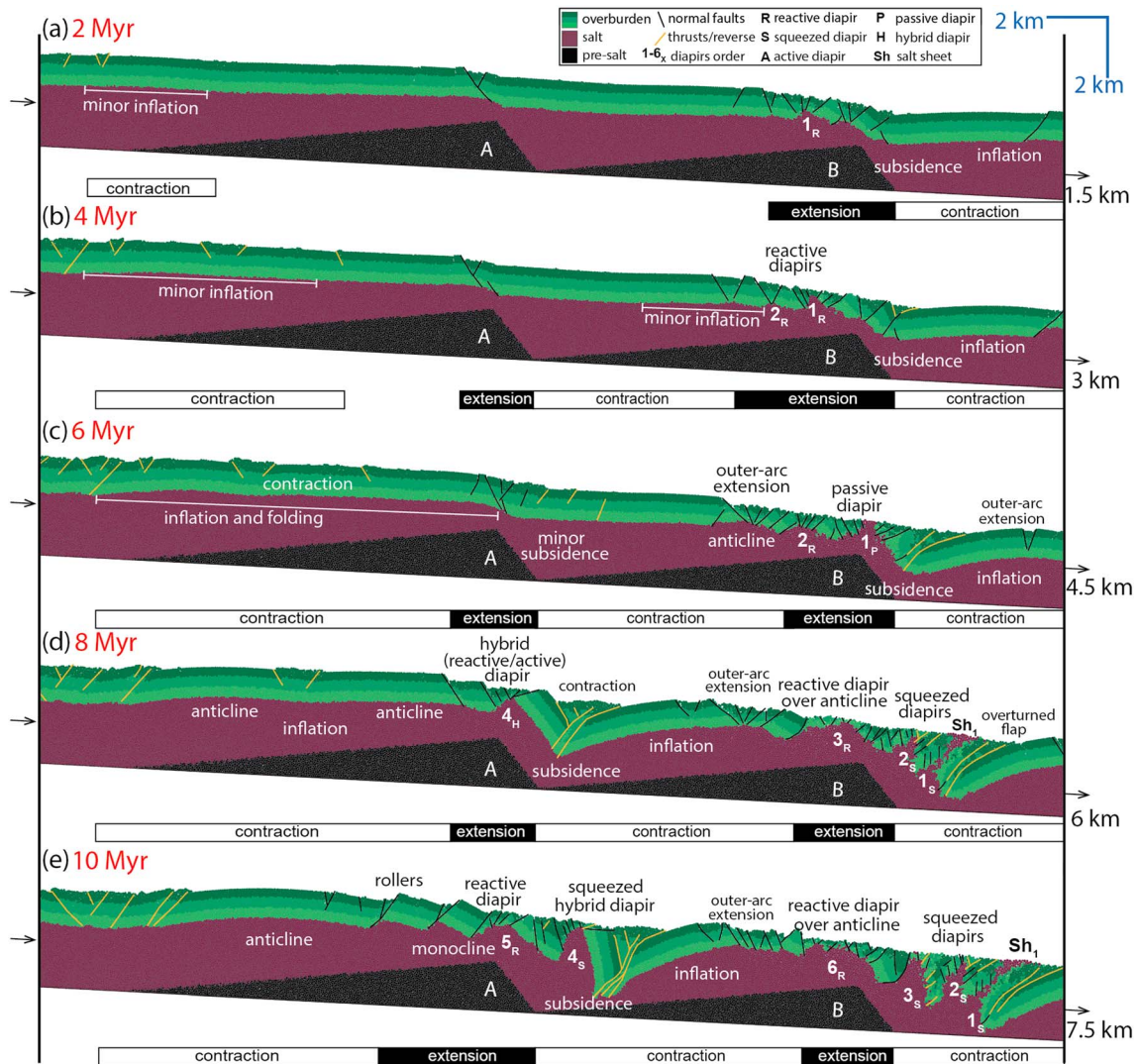
Figure 4. (a-e) Sequential evolution shown in increments of 2 Myr of Model B: Basinward-dipping normal faults, simulating translation over tilted fault-blocks (A and B). Each of these blocks defines a gentle landward-dipping base-salt ramp and a steep basinward-dipping base-salt ramp. To improve visualization of relevant structures only the centre of the model is shown. Salt flux variations occur above each ramp segment complicating flow kinematics and overburden deformation. As the system translates, structures move over different structural domains, being reactivated and/or inverted. Extensional (black boxes) and contractional (white boxes) domains occur over each fault-block, which change through time. Diapirs are represented by numbers 1–6 and their corresponding style of growth in subscript. A salt sheet (S1) forms due to diapir squeezing at the bottom of the distal basinward-dipping ramp.

By 10 Myr (Figure 4e), the earlier-formed updip anticline was amplified over Footwall A as it approached its crest (Figure 4d-e). The intermediate anticline (Figure 4d) moved over the extensional hinge at the top of Fault A, being unfolded into a monocline and extended by a series of landward-dipping normal faults (Figure 4e). The earlier-formed hybrid diapir (4_H, Figure 4d) moved across Fault A, rising and upturning its flanks further as it became squeezed over Footwall B (4_S, Figure 4e). The downdip anticline was also further contracted and amplified as it translated over Footwall B (Figure 4e). A new reactive diapir (6_R, Figure 4e) formed on the downdip limb of this anticline as it reached the extensional hinge above the footwall crest of Fault B. The earlier-formed reactive diapir (3_R, Figure 4d) moved over the contractional hinge at the base of Fault B where it was squeezed and rose further (3_S, Figure 4e). Due to their greater width (1.5–3 km), diapirs 2_S and 3_S did not weld like the oldest, narrower (< 1 km) diapir (1_S, Figure 4e), which remained broadly unchanged as it lost its connection with the source-layer at an earlier stage (Figures 4d-e).
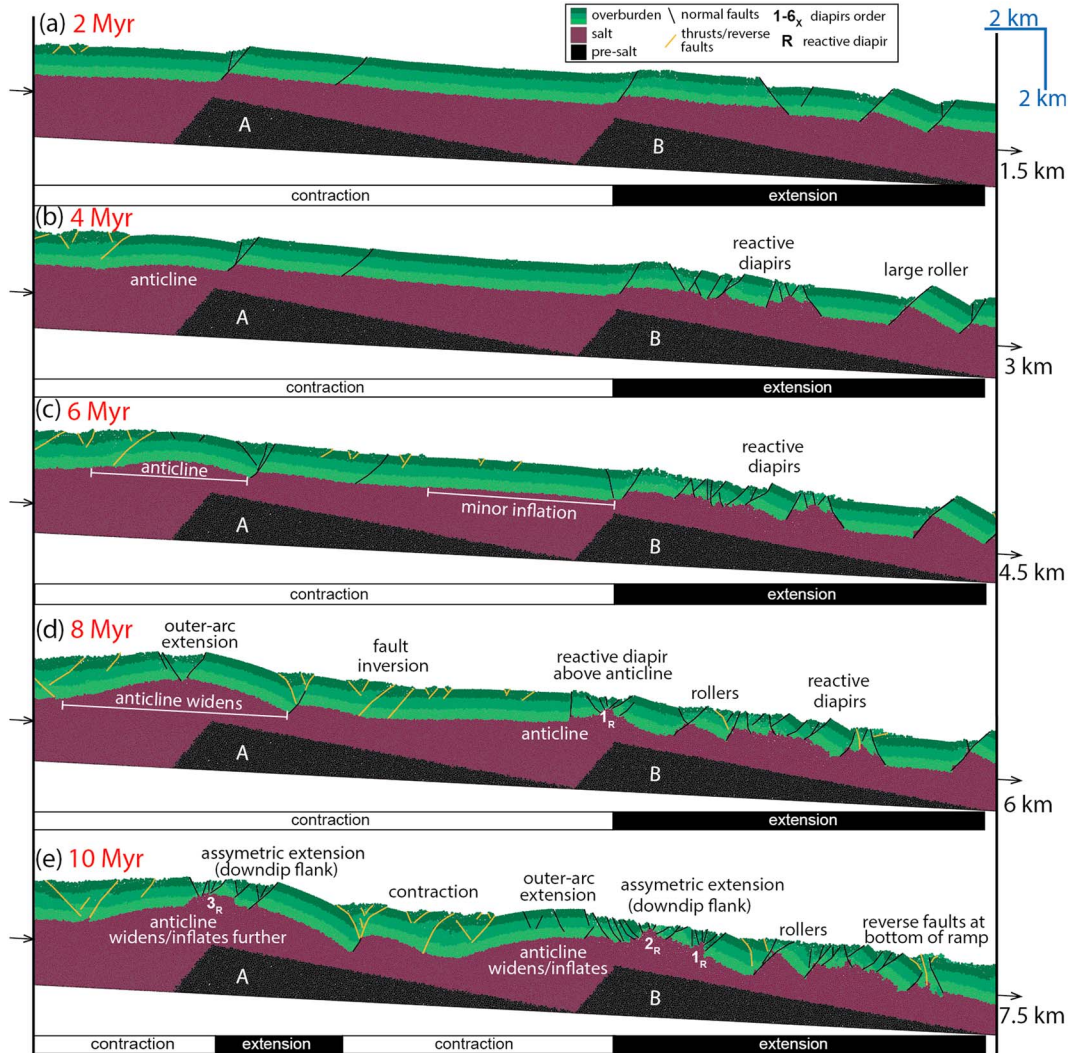
Figure 5. (a-e) Sequential evolution presented in increments of 2 Myr of Model C: Landward-dipping normal faults, which simulates salt-detached translation over a pair of tilted fault-blocks defining steep landward-dipping base-salt ramps updip and gentle basinward-dipping base-salt ramps downdip. To improve visualization of relevant structures at the centre of the model, its edges are not shown. Contractional (lower white boxes) domains and extensional (lower black boxes) occur over each half-graben by the end of the experiment. Diapirs are represented by numbers 1–3 and their corresponding style of growth in subscripted letters.

5. Pre-Salt Tilted Fault-Blocks With Landward-Dipping Normal Faults (Model C)

In this model, Faults A and B define steep base-salt ramps dipping oppositely (i.e. landward) to the flow direction and, thus, act as strong barriers to basinward salt flow, enhancing updip salt inflation and contraction, ultimately leading to the development of large salt anticlines above them (Figure 5). The footwalls (A and B) act as gentle and wide basinward-dipping base-salt ramps that locally favor gliding, leading to extension and, particularly over Footwall B, the development of normal faults, reactive diapirs and salt rollers (Figure 5). Extension is markedly less over Footwall A because it is located between the two landward-dipping faults that obstruct salt flow.

From 0–6 Myr (Figure 5a-c), continuous translation increases salt flux mismatches and inflation over Fault A widening the updip anticline, which moves partially into the footwall crest of Fault A. This produces minor flux variations over Footwall A and, consequently, mild extension of the anticline updip and downdip shortening with the development of a wide zone of inflation as flow is buttressed against Fault B (Figure 5c). By 8 Myr, the zones of inflation over faults A and B are amplified and widened further, being affected by

significant outer-arc stretching (Figure 5d). A reactive diapir (1_R, Figure 5d) forms above the inflated salt over Fault B as this zone expands and begins to be influenced by gliding and extension down Footwall B. The anticline formed over Fault A, however, is only locally extended by outer-arc stresses because downdip translation over Footwall A is buttressed by Fault-block B producing greater inflation and contraction over the entirety of Fault-block A (Figure 5d). By the end of the experiment, both anticlines thicken and widen, extending asymmetrically on their basinward flanks as they move over the extensional hinges on the footwall crest of both faults (Figure 5e). The anticline above Fault A is asymmetrically extended, with greater extension on its basinward side above Footwall A, and a reactive diapir develops at its crest as it moves beyond Fault A (3_R, Figure 5e). Over Fault-block B, the reactive diapir (1_R, Figure 5e) translates down and away from the footwall crest where it originated, and a new reactive diapir nucleates at that point (2_R, Figure 5e).

6. Effects of Step Height and Connectivity Between Sub-Basins

In this set of experiments, we test the effects of pre-salt structural relief and the associated variable salt thickness and connectivity across sub-basins defined by basinward- and landward-dipping normal faults by varying the height of the central footwall-crest (Table 1, Figures 2d-e, 6a-d and 7a-d). In the models with the largest structural relief (models B4 and C4, Table 1, Figures 6d and 7d), there is no salt over the footwall crest so the sub-basins are initially disconnected.

In both cases of sub-basins, salt flux mismatches are driven by and directly proportional to the base-salt relief and associated salt thickness contrasts across sub-basins. For basinward-dipping pre-salt normal faults (Figure 6), an increase in the footwall crest height results in greater buttressing and salt inflation over the footwall (i.e. base-salt landward-dipping ramp), and greater salt thinning and cover subsidence above the fault (i.e. base-salt basinward-dipping ramp) (Figure 6a-c). Flux mismatches are, therefore, enhanced where salt is thinner over fault crests (Figure 6). The magnitude and width of inflation increase progressively as the height of the footwall crest increases (from 1.2 to 2.1 km, Figure 6a-d). As cover subsidence and salt thinning are also intensified over the larger normal fault scarps, the width of associated extensional and contractional zones, the number of normal faults, and intensity of reactive diapirism also increase (Figure 6a-c). The locus of maximum subsidence remains closer to the base of the fault scarp as the pre-salt step height increases and, consequently, the connectivity between sub-basins decreases (Figure 6).

These relationships do not completely apply where salt sub-basins either side of the normal fault were initially disconnected due to greater pre-salt topography. In this scenario, extension and contraction are more localized, and marked salt attenuation and welding occurs over the fault (Figure 6d). A narrow zone of extension forms due to gliding and salt thinning over the fault, which passes immediately downdip to a wider area of contraction above the base of the fault and into the downdip fault-block (Figure 6d). A salt sheet advances over the footwall crest from the updip sub-basin over thinned salt of the downdip sub-basin, developing another set of extensional and contractional structures above it (Figure 6d). Gradual translation and inflation over the footwall crest allows the salt to build enough gravitational instability, causing it to advance basinward by thrusting over the extensionally thinned salt in the downdip sub-basin (Figure 6d). Once the salt advances over the downdip sub-basin, however, these initially isolated systems no longer evolve independently as the sheet and its roof impose additional structural loading onto the downdip sub-basin, amplifying salt expulsion over the border fault and inflation further downdip (Figure 6d).

In landward-dipping pre-salt normal fault systems, the base-salt relief associated with the fault dips steeply and in the opposite direction to the salt flow, therefore acting as a strong barrier to downdip translation (Figure 7). As a result, the magnitude of salt inflation, overburden contraction and uplift is larger for greater faults (Figure 7a-c), except in the case of disconnected sub-basins (Figure 7d). The observed zone of inflation is located progressively landward as footwall crest height increases, because the salt has greater difficulty flowing across higher relief steps, remaining pinned above them for a longer time (Figure 7a-d). As a result, fewer and smaller reactive diapirs nucleate over the inflated salt for models with higher footwall crests (Figure 7a-c). In a similar way to the basinward-dipping faults model (Figure 6), when the salt sub-basins are initially isolated they evolve independently until the salt inflates enough above the footwall crest that it becomes able to advance by thrusting basinward over previously thinned strata in the downdip sub-basin (Figure 7d).
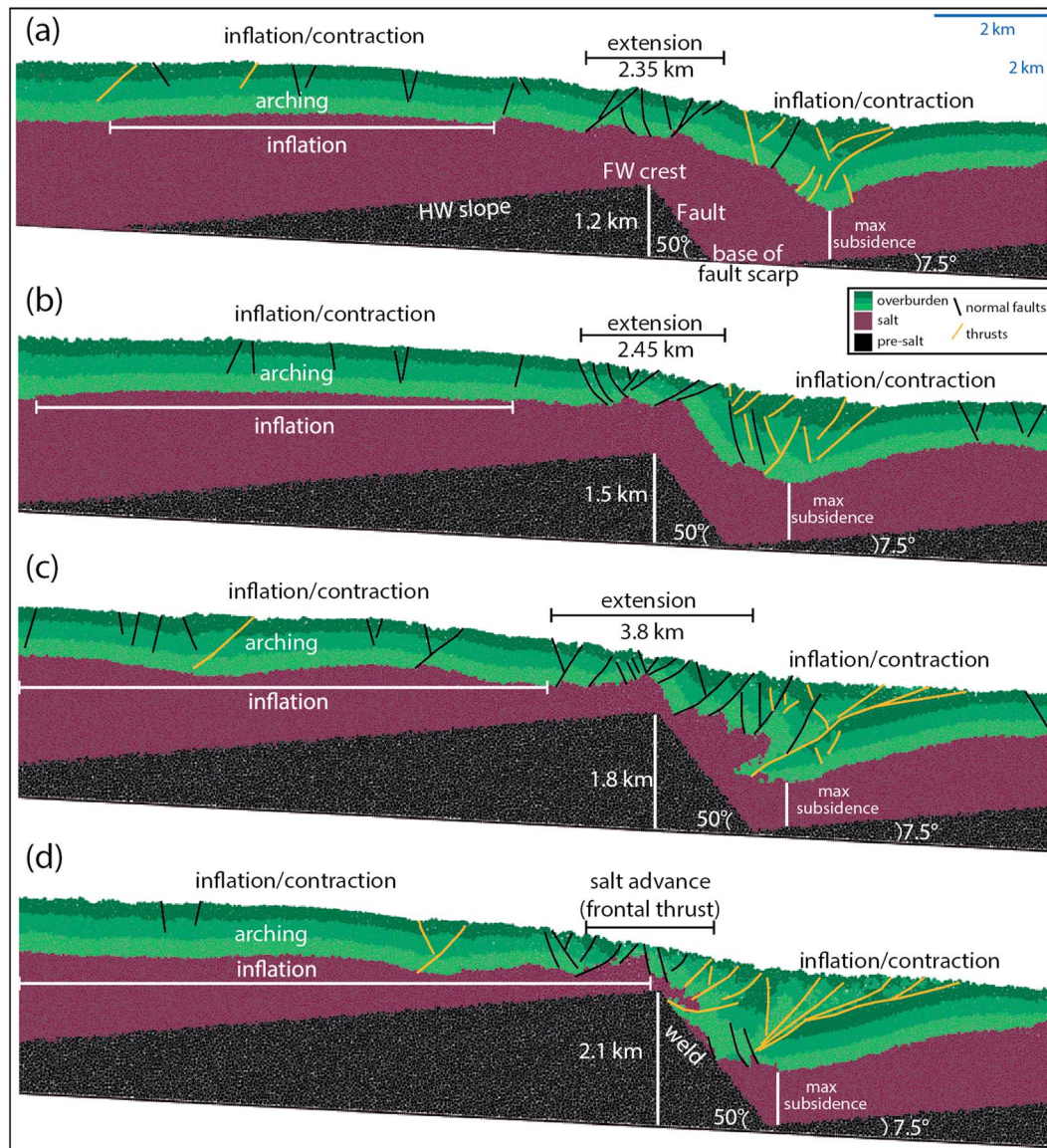
Figure 6. Final results (after 10 Myr) showing the effects of salt connectivity and pre-salt step height on lateral salt flow, diapirism and overburden deformation for tilted fault-blocks defined by basinward-dipping faults: (a) B1, (b) B2, (c) B3, and (d) B4. Maximum salt thickness in all models is 2.1 km at the deepest portion of the graben and minimum salt thickness is of 900 m (B1), 600 m (B2), 300 m (B3) and 0 m (B4) over the pre-salt structural highs. Model boundaries are far from the section of the model shown so structures are not affected by boundary artifacts. Zones of updip inflation are shown by white horizontal lines and zones of extension by black horizontal lines. Normal faults are in black and reverse faults in orange.

7. Discussion

7.1. Effects of Pre-Salt Rift Geometries on Salt Flow and Overburden Deformation

The horst model (Model A) reproduces a similar dynamic evolution and distribution of structural styles to the physical models of Dooley et al. (2017; 2018) (Figures 1b, 8a and 9a). Translation and the associated variations in the cross-sectional area of flow across a pre-salt horst result in salt inflation over the updip edge of the horst and salt thinning over its downdip edge (Figure 8a and 9a). A salt anticline forms over the updip edge of the horst and, as it progressively thickens and widens, it moves onto the crest of the horst where it collapses and extends (Figures 3 and 8a). In contrast, over its downdip, basinward-dipping edge, a monoclinal zone of subsidence develops and is characterized by extension and reactive diapirism above the pre-salt footwall crest, and contraction and diapir squeezing at the base of the pre-salt fault (Figures 3 and 8a).
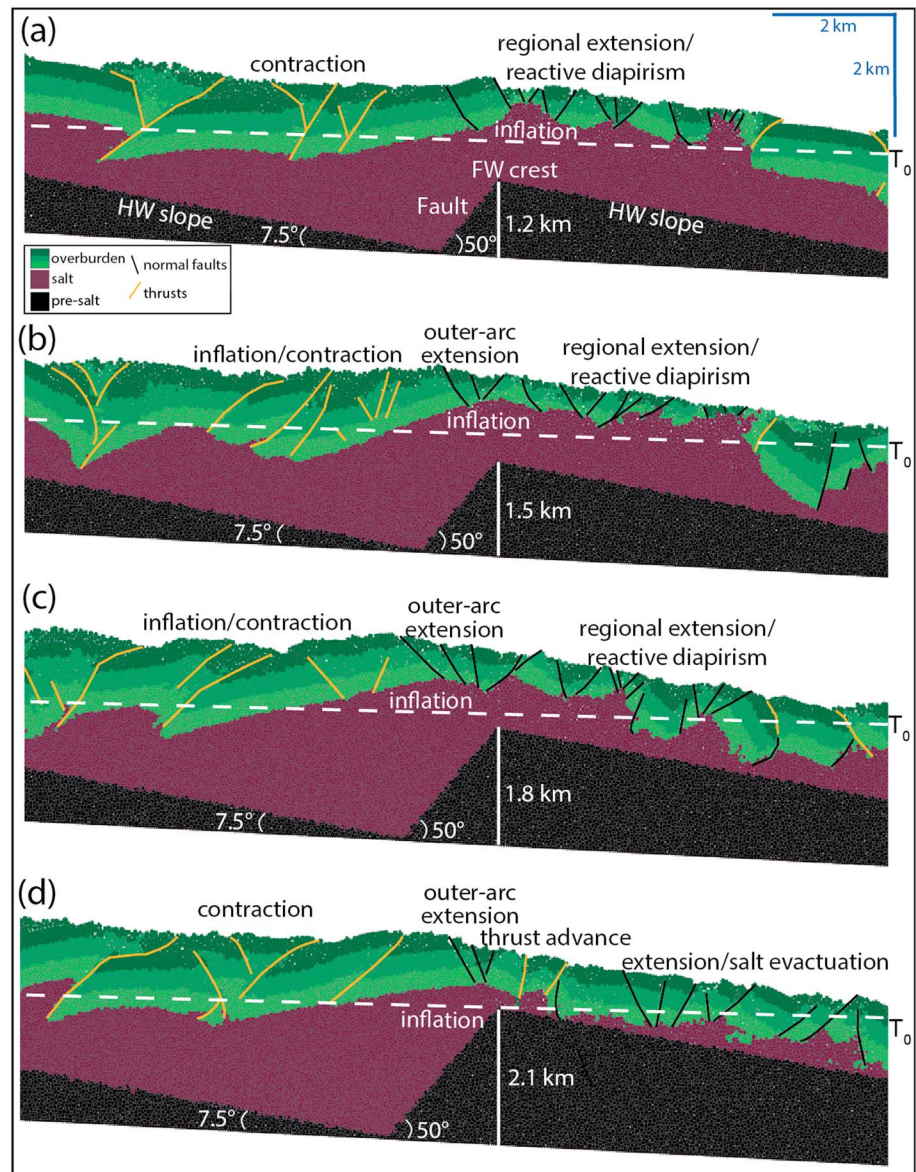
Figure 7. Final (after 10 Myr) results showing the effects of salt connectivity and pre-salt step height on lateral salt flow, diapirism and overburden deformation for tilted fault-blocks defined by landward-dipping faults: (a) C1, (b) C2, (c) C3, and (d) C4. Maximum salt thickness in all models is 2.1 km at the deepest portion of the graben and minimum salt thickness is of 900 m (B1), 600 m (B2), 300 m (B3) and 0 m (B4) over the pre-salt structural highs. White dashed-lines represent original top salt (T0). Model boundaries are far from the section of the model shown so structures are not affected by boundary artifacts. Zones of inflation are indicated by white dashed lines. Normal faults are in black and reverse faults in orange.

Tilted fault-block models (Figures 4–7) demonstrate how translation across sets of steep and gentle base-salt ramps associated with syn-rift normal faults and footwalls result in more complex patterns of overburden deformation and diapirism. This occurs because the salt flux varies more frequently and abruptly as it is influenced by greater changes in base-salt relief (Figure 8b-c and 9b-c).

In models where salt and overburden translate across tilted fault-blocks defined by basinward-dipping normal faults (Model B, Figures 4 and 8b), wide zones of salt inflation and overburden contraction develop over the gentle landward-dipping base-salt ramps above their footwalls (Figures 8b and 9b). This occurs because initial salt thickness decreases towards the footwall crest and, with downdip translation, the cross-sectional area of salt arriving at that point is larger than that leaving (Figure 9b). Conversely, the

Figure 8. Synthesis diagram of final model results comparing structural style distribution associated with (a) a pre-salt horst, and pairs of tilted fault-blocks defined by (b) basinward-dipping and (c) landward-dipping pre-salt rift faults. (S) Indicates zones of subsidence and (I) zones of inflation and contraction. The distribution of structural domains is shown at the bottom of each section with extensional domains in black boxes and contractional domains in white boxes. Normal faults are shown in black and reverse faults in red. Pre-salt rift structures are in black, salt in pink and overburden in light green.

cross-sectional area of salt leaving the basinward-dipping normal fault is greater than that arriving at its footwall crest, which generates a monoclinal zone of subsidence over the fault defined by extension above its crest and contraction over its base (Figures 4, 8b and 9b). This structural style is similar to that developed downdip of the horst (Model A), but it is narrower and more complex due to the influence of adjacent oppositely-dipping base-salt ramps (Figures 8a-b). As translation continues, deformation intensifies with the zones of extension and contraction expanding landward and basinward respectively (Figure 4). Salt anticlines developed above the footwall translate over the footwall crest and become extended and pierced by reactive diapirs (Figures 4 and 8b). Extensional structures (i.e. normal faults and reactive diapirs) initially formed near the footwall crest (i.e. extensional hinge) translate over the base of the fault scarp where flow decelerates (i.e. contractional hinge), and are rotated, inverted, and/or squeezed (Figures 4, 8b and 9b). This pattern repeats for each fault-block encountered resulting in more abrupt transitions, overlap and alternation of contractional and extensional domains relative to settings without or with simpler base-salt relief, e.g. horst blocks (Figure 8a-b).

Where tilted fault-blocks are defined by landward-dipping normal faults (Model C), intense obstruction of salt flow and, thus, greater salt inflation and contraction are observed against and above the normal fault (Figures 5, 8c and 9c). This results in higher-amplitude, but narrower zones of inflation and contraction compared with the basinward-dipping normal fault model (Figures 8b-c). Additionally, the presence and proximity of two barriers to basinward salt flow associated with the underlying landward-dipping faults results in overall greater magnitudes of shortening and reduced extension and subsidence between the two fault blocks when compared to the other models (Figures 8 and 9). As translation continues, salt anticlines become progressively wider and thicker, eventually moving across the footwall crest and over the gentle basinward-dipping footwall (Figures 5 and 8c). As a consequence, the anticlines are asymmetrically extended and pierced by reactive diapirs, with greater extension occurring on their downdip limb over the basinward-dipping footwalls (Figures 5 and 8c). However, as regional contraction does not favor diapirism as much as extension (Vendeville & Jackson, 1992, 1994), translation over pre-salt fault-blocks defined by landward-dipping normal faults results in considerably less diapirism than in other settings (Figure 5 and 8).
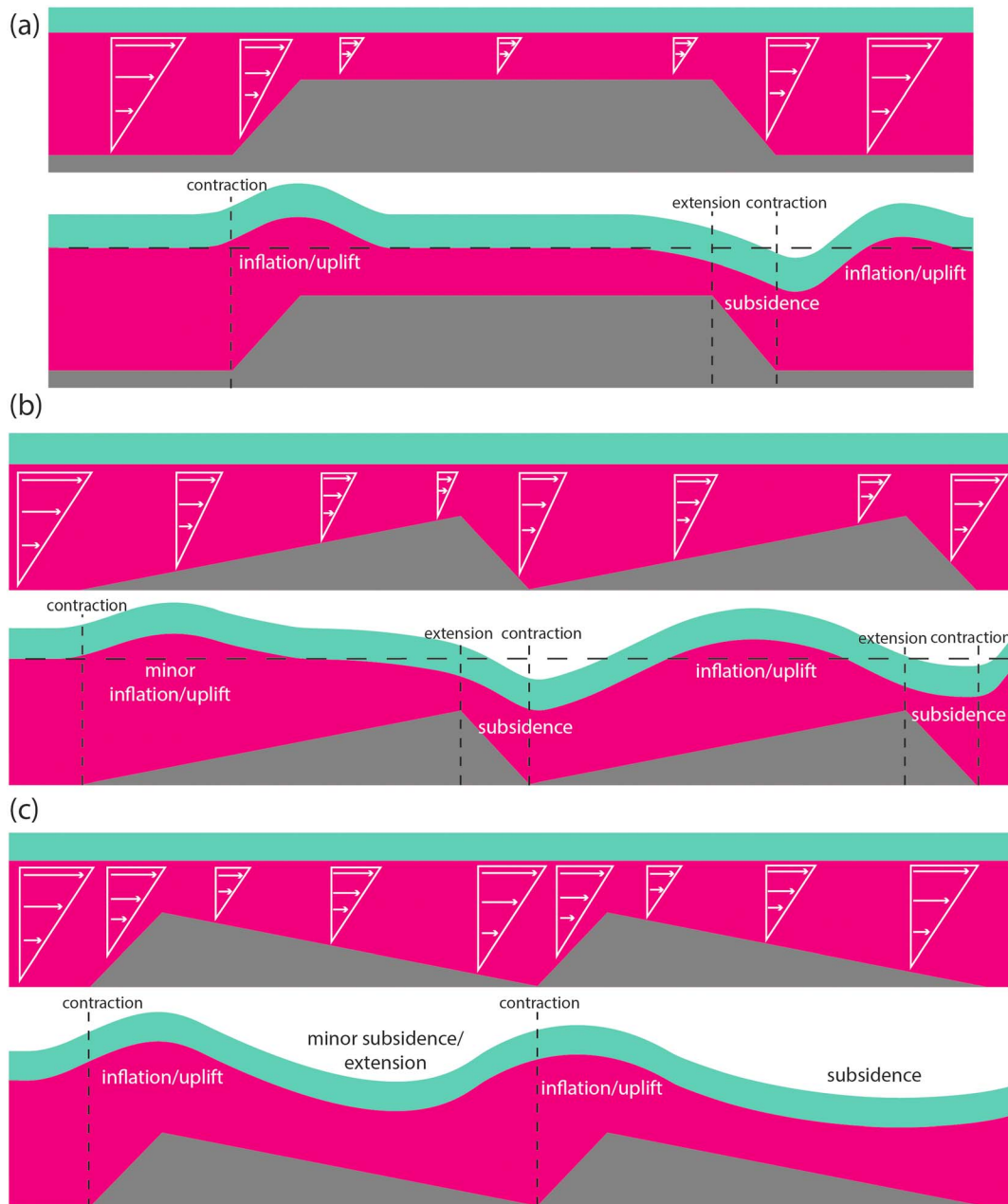
Figure 9. Simplified diagram based on model results illustrating initial salt structures and the dynamics of viscous shear (Couette salt flow) and flow perturbations related to gliding and salt flux changes due to variations in original salt thickness across pre-salt topography: (a) pre-salt horst; and pairs of tilted fault-blocks defined by (b) basinward-dipping and (c) landward-dipping pre-salt rift faults.

Our experiments confirm the hypothesis that pre-salt structures and base-salt topography are responsible for nucleating salt structures by promoting changes in salt flow and overburden deformation patterns (Deptuck & Kendell, 2017; Dooley et al., 2017; 2018; Ge et al., 1997; Pichel et al., 2018) (Figures 3–5). As translation progresses, salt and overburden structures eventually leave the pre-salt topography where they originated and are reactivated downdip by the next pre-salt structure encountered (Figures 3–5). These early-formed structures act as weakness zones that may be eventually exploited and amplified by later processes such as loading or tectonic reactivation, further complicating the evolution of these systems and our ability to interpret them (Dooley et al., 2018).

The models presented here reproduce a wide range of diapirism styles (i.e. reactive, passive and active, Hudec & Jackson, 2007) (Figures 3–5, 8 and 10a-b), along with small salt sheets formed by extrusion and
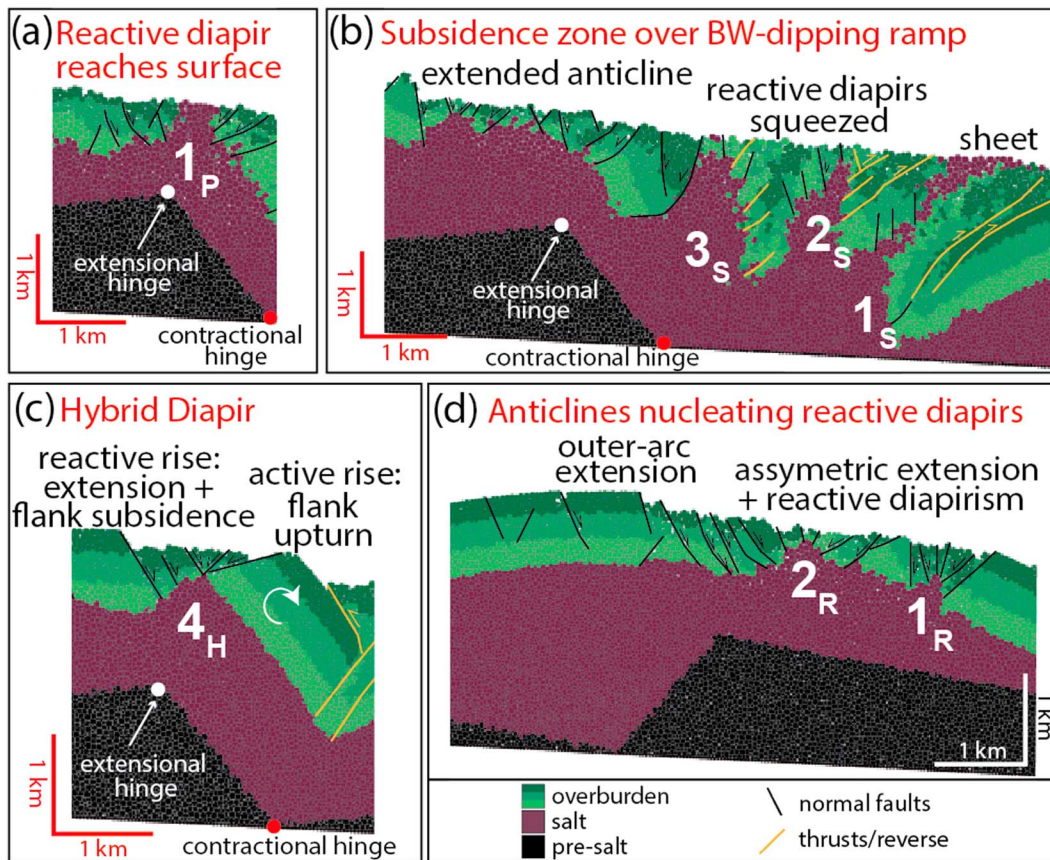
Figure 10. Focused sections showing examples of salt response and complex, multiphase styles of diapirism associated with flow over base-salt ramps. (a) after continuous extension, a reactive (i.e. extensional) diapir reaches the surface and continues to evolve as a passive diapir (1_P) at an extensional hinge at the crest of a basinward-dipping normal fault of Model B (4 Myr). (b) Reactive diapirs are squeezed (1_S, 2_S and 3_S) and normal faults inverted as they move over the base of the basinward-dipping (BW) fault (contractional hinge) with salt sheet extruding from the crest of the basinwardmost diapir (1_S) in Model B (10 Myr). (c) Hybrid diapir characterized by extension and reactive rise over the footwall crest (extensional hinge) and active diapirism and flank upturn over the base of the fault (contractional hinge) in Model B (8 Myr). (d) Salt anticline inflates over a landward-dipping fault whilst its downdip flank collapses, being extended and pierced by reactive diapirs over the basinward-dipping dip-slope in Model C (10 Myr).

thrusting (Figures 4, 6 and 10b). Positioning of a salt structure over distinct base-salt domains results in complex, hybrid diapir growth in which one of its flank undergoes extension while the other is in contraction (Figures 3–5, 10c-d). This occurs because the salt structure (i.e. diapir or anticline) is simultaneously influenced by contrasting flux variations and, thus, velocity mismatches (c.f. Dooley et al., 2017), and variable stress regimes on its flanks when these are located over distinct base-salt domains. Anticlines inflate over base-salt landward-dipping ramps whilst being asymmetrically extended and pierced by reactive diapirs over basinward-dipping ramps (anticline over Fault-block B in Figure 4d-e and updip anticlines in Figures 3, 5 and 10d). Conversely, a diapir rises by extension over the footwall crest of basinward-dipping faults whilst actively piercing and upturning its roof above the base of the fault (hybrid diapir, Figure 4d and 10c). This phenomenon has been briefly described in an area of thick salt and prominent base-salt relief in the Santos Basin (Pichel et al., 2018), and may also be recognized over allochthonous salt in the Gulf of Mexico (Duffy and Peel pers. comm. 2018).

Salt flux variations and associated overburden deformation are driven primarily by shear-drag within the salt (i.e. Couette-flow, c.f. Dooley et al., 2017; Pichel et al., 2018), a process also illustrated in dynamic models based on our experiments (Figure 9a-c). Earlier numerical simulations reproducing viscous salt drag and overburden translation (SaltDragON, Peel©) exhibit remarkably similar kinematics associated with simpler flat-ramp systems (Pichel et al., 2018). These earlier models accurately simulate salt flux variations, sedimentation and development of asymmetric minibasins, i.e. ramp-syncline basins (Pichel et al., 2018), but do not reproduce lateral overburden deformation (i.e. extension and contraction) nor diapirism. The models

presented here complement this earlier work by showing the effects of non-uniform translation over complex base-salt relief, with resultant overburden contractional and extensional deformation (i.e. folding, faulting) and diapirism. These are, nonetheless, simplifications of salt flow in nature, which is typically hybrid and simultaneously affected by varying proportions of Couette and Poiseuille flow components (Pichel et al., 2018; Rowan et al., 2004; Weijermars et al., 2014).

Variable pre-salt structural relief and sub-basin connectivity have a significant impact on flow kinematics and overburden deformation. Higher pre-salt fault topography and associated differences in salt thickness across neighboring sub-basins produce stronger buttressing, flux variations and flow disruptions. This produces greater updip inflation and contraction over landward-dipping base-salt ramps, and greater downdip subsidence and associated extension and contraction over basinward-dipping base-salt ramps (Figures 6, 7). In cases where sub-basins are initially disconnected, they evolve independently until inflated salt from the updip fault-block is able to advance basinward into the downdip fault-block by thrusting (Figure 6d and 7d). In these cases, the final observed distribution of extensional and contractional strain is more localized and repeated on each sub-basin (Figures 6d and 7d). The width and magnitude of localized strain provinces is proportional to the width and steepness of the base-salt ramps that they are associated with (Figures 4–8). Steep and narrow ramps, which in our models are associated with normal fault scarps, result in stronger, more abrupt salt flux changes and deformation over a narrower region. Gentle and wider ramps, associated with footwall dip-slopes, produce deformation that is subtler, but distributed over a wider area (Figures 4–8).

7.2. Applicability and Comparison With Seismic Examples

The models have limitations associated with free-edge effects and moving boundaries (c.f. Hardy & Finch, 2005; Pichel et al., 2017). Small-scale structures and the degree of faulting might differ locally from natural examples as these are affected by other variables not modeled here, e.g. changes in sedimentation pattern, loading, intra-salt stratigraphy, and tectonic reactivation. Nonetheless, our models produce salt flux variations, diapirism and distribution of structural styles similar to most recent physical experiments (Dooley et al., 2017; 2018) (compare Figure 1b and 8a), and examples of syn- and post-rift salt basins (Figures 11 and 12). The benefits of using DEM to model translation and salt flux variations over significantly variable base-salt topography are that results are easily reproducible and afford analysis of the sequential evolution of highly-strained systems and diapirs in cross-section. This is crucial to understand the distribution of salt and overburden geometries that undergo a complex, multiphase history of extension and contraction. Discrete-element models (DEM) cannot substitute finite-element models (FEM) or physical models as these methods have other advantages; but the DEM technique applied here complements these other approaches improving the understanding of regional salt tectonics.

Results presented here are especially applicable to late syn-rift salt basins, which are mainly affected by thin-skinned salt tectonics and present wedge-shaped salt sequences across half-grabens (Jackson & Hudec, 2017; Rowan, 2014). Examples of these basins include Nova Scotia (Figure 11) (Albertz & Ings, 2012; Deptuck & Kendell, 2017), offshore Morocco, Mauritania (Davison, 2005; Tari & Jabour, 2013; Tari et al., 2017) and the Red Sea (Mitchell et al., 2010; Rowan, 2014). Additionally, initial basin geometries used in these models can also be applicable to segments of post-rift salt basins where significant base-salt topography is inherited from previous phases of rifting. Examples include Santos (Figure 12) (Davison et al., 2012; Pichel et al., 2018); Campos (Davison et al., 2012; Dooley et al., 2017), Kwanza and Lower Congo (Hudec & Jackson, 2004; Jackson and Hudec, 2005; Peel 2014); and Gulf of Mexico (Dooley & Hudec, 2017; Hudec et al., 2013).

As seen in examples of syn-rift salt from Nova Scotia, at the top of pre-salt faults and footwalls that define basinward-dipping base-salt ramps, deformation is characterized by extension (i.e. salt rollers and normal faults, Figure 11). Conversely, at the base of basinward-dipping faults and/or over landward-dipping faults or footwalls, deformation is characterized by salt inflation and contraction, which are evidenced by fault inversion and thrusting (Figure 11a), and diapir squeezing (Figure 11b).

In the case of post-rift salt in the Santos Basin, variations of base-salt relief are less pronounced, but the strain and structural style distribution are remarkably similar to the models presented here (Figure 12). Salt anticlines form by contraction (indicated by intra-salt seaward-vergent shear zones) above landward-dipping base-salt ramps, and are later asymmetrically extended by basinward-dipping normal faults above a
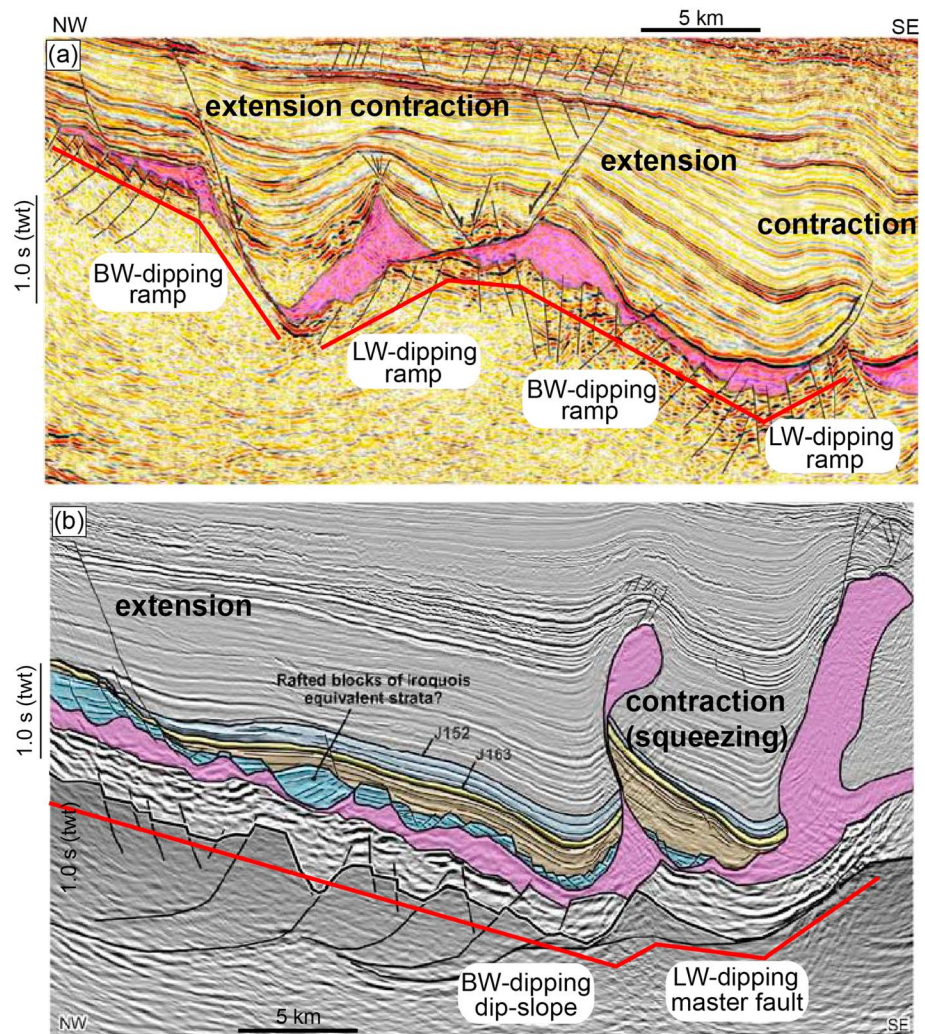
Figure 11. Seismic examples of the impact of complex pre-salt syn-rift topography on salt tectonics of a late syn-rift salt basin in Nova Scotia (modified from Deptuck & Kendell, 2017). (a) Movement over a pair of steep basinward- (BW) and landward (LW)-dipping ramps produces extension at the top of the basinward-dipping ramp and simultaneous contraction and uplift at its bottom and over the landward-dipping ramp. Further downdip, another zone of extension and salt expulsion occurs at the top of a gentle basinward-dipping step while a previous extensional minibasin is translated basinward, being contracted at the bottom of this ramp and over a small landward-dipping step. (b) Extension occurs at the top of a gentle basinward-dipping ramp; while a previously reactive/passive diapir formed further updip is squeezed as it is buttressed against a steep landward-dipping pre-salt step. Red lines below salt interval indicate the large-scale base-salt geometries.

broadly flat base-salt high (Figure 12a-b). Deformation over most of this horst is dominated by extension and widening of earlier salt anticlines, and reactive diapirs characterized by a triangular shape and inward-dipping and younging normal faults (Figure 12a-c). Minor later inflation occurred as structures approached a subtle landward-dipping base-salt ramp near the horst margin as indicated by an earlier reactive diapir that later uplifts a broadly tabular roof (Figure 12c). Above the large basinward-dipping base-salt ramp defined by a set of basinward-dipping normal faults, deformation is characterized by a monoclinal zone of subsidence (Figure 12a). This zone of subsidence is characterized by updip extension and downdip contraction similar to models presented here (Figures 9 and 12). An earlier salt anticline is extended at the crest of this ramp (Figure 12d), while a fold-thrust belt develops at and downdip of its base (Figure 12e).

Models simulating variable base-salt ramp height (Figures 7, 8) help to understand along-strike variations of salt-related structural styles on rifted margins due to variability in the pre-salt rift geometry associated with
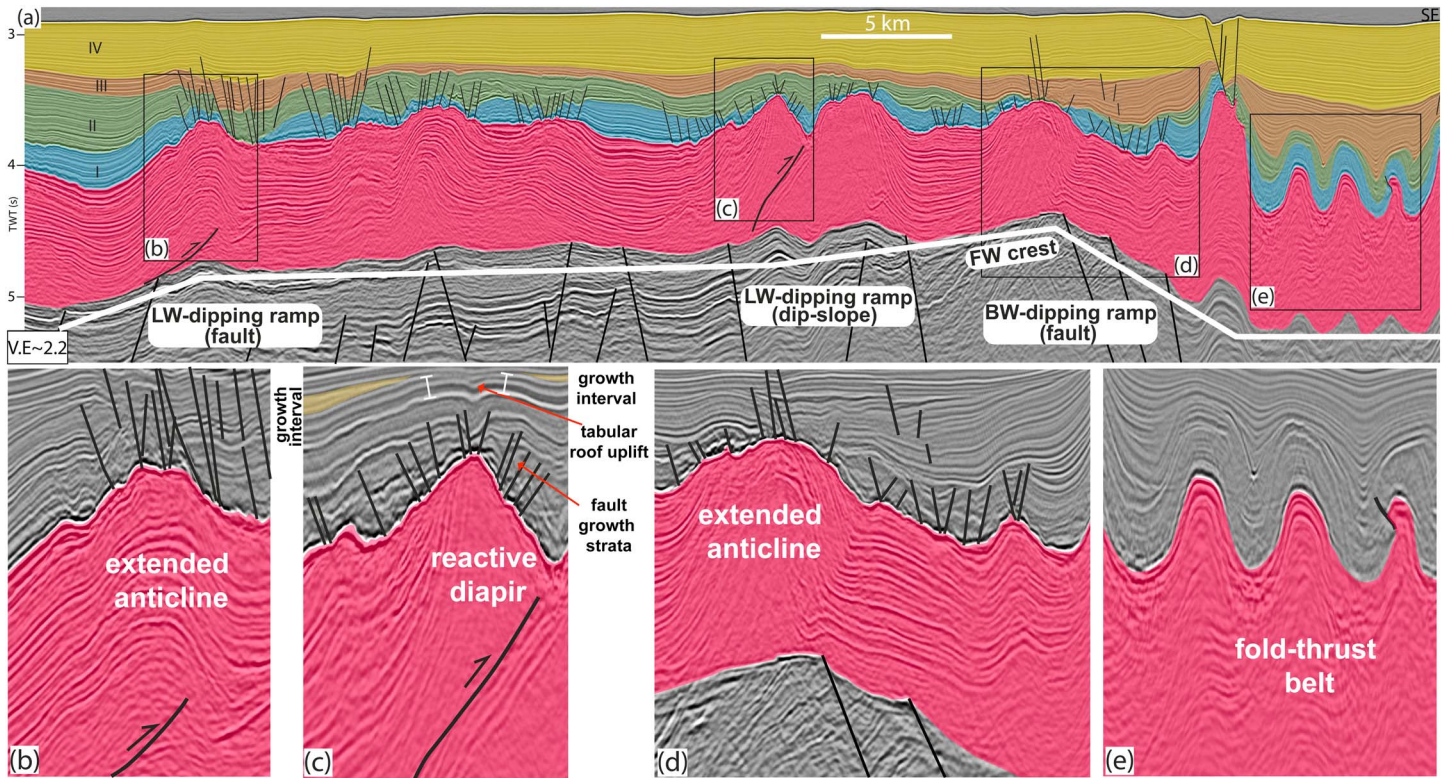
Figure 12. (a) High-resolution regional seismic section illustrating the effects of complex pre-salt relief on salt flow in a post-rift salt basin, Santos Basin, Brazil. Salt is on average 2 km thick and has a prominent intra-salt layering, which works as a kinematic indicator. (b)-(e) close-ups. (b) Movement over a landward-dipping base-salt step results in contraction (evidenced by a basinward-vergent intra-salt shear zone) and development of a salt anticline that is asymmetrically extended above the base-salt high. Over the pre-salt horst, deformation is driven mainly by extension and reactive diapirism. (c) Close-up of reactive diapir shows growth strata associated to normal faults and later uplift of a tabular roof with growth strata in yellow. At the downdip edge of the tilted fault-block, movement over the pre-salt footwall crest (FW crest) and basinward-dipping fault produces a zone of extension at the top (d) and contraction (fold-thrust-belt) at its base (e).
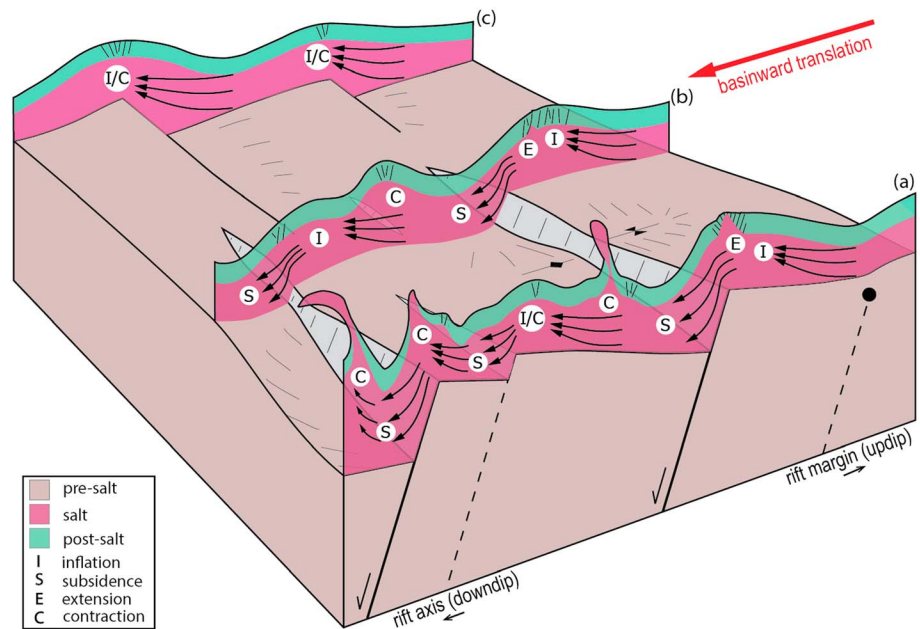

Figure 13. Along-strike variation of salt structural domains linked to pre-salt rift topography associated with fault segmentation, throw variations and dip polarity typical of rift settings (rift template based on Gawthorpe & Leeder, 2000). Profile (a) shows variations related to high-relief as well as closely-spaced basinward-dipping rift faults, whereas profile (b) illustrates variations associated with low-relief basinward-dipping faults and profile (c) landward-dipping faults.

normal fault throw, segmentation, spacing and polarity (Figure 13). An increase of throw towards the centre of basinward-dipping faults results in greater inflation over the footwalls and subsidence above the faults with, consequently, greater extension at the footwall crest and contraction at the base of the fault (Figure 13a). Thus, greater base-salt relief, usually near the centre of syn-rift faults, can produce increased salt rise and diapirism (Figure 13a), whereas towards the fault tips, structures tend to be more subtle and dominated by salt subsidence and inflated anticlines (Figure 13b). Closely spaced fault-blocks generate more abrupt flux variations, depending on the base-salt relief they generate. For closely spaced, basinward-dipping fault blocks, there is an increase in the buttressing effect at the base of the fault and against the landward-dipping footwall, amplifying contraction and squeezing of earlier structures (left-hand side, Figure 13a). Buttressing and contraction are also increased in the case of reversed fault polarity (i.e. landward-dipping faults) producing larger salt anticlines but, due to less extension of the overburden, less diapirism than above basinward-dipping faults (c.f. Figure 13a and c).

8. Conclusions

The models presented here reproduce salt flux variations and structural styles associated with salt and over-burden translation across pre-salt topography that are similar to recent physical experiments (c.f. Dooley et al., 2017; 2018). Our numerical modeling results complement and expand on these previous studies by investigating the cross-sectional sequential evolution and multiphase diapirism in these settings, and testing the influence of a more complex and realistic pre-salt structural framework of connected variably-dipping base-salt ramps. These models do not intend to simulate the entire lateral extent and temporal evolution of salt basins, rather they focus on illustrating how pre-salt relief nucleates salt structures and influences their evolution by disrupting early salt flow.

Base-salt ramps with variable slopes related to tilted fault-blocks and their bounding normal faults produce higher-frequency variation of structural styles and diapirism than in simpler flat-ramp base-salt systems defined by pre-salt horsts. As salt and cover move downdip, structures translate over contrasting structural domains, being inverted and/or growing asymmetrically. Gliding over tilted-blocks defined by basinward-dipping normal faults produces wide, low amplitude zones of inflation above footwalls, and abrupt, narrow zones of subsidence over steep fault-scarps. Reactive diapirs form near the footwall crest, and become squeezed, potentially extruding salt sheets as they move across the fault. Translation over tilted-blocks defined by landward-dipping faults produces narrow zones of inflation over the steep fault-scarp, with overall greater contraction and less diapirism as flow is obstructed by ramps dipping contrary to flow direction. Results also demonstrate how variable height, dip and orientation of pre-salt structures play a key role on the evolution of these systems and can partially explain along-strike variation of salt-related deformation in rifted margins.

The modeled geometries and distribution of structural styles are comparable to seismic examples of both syn- and post-rift salt basins where prominent base-salt relief exists. Additionally, the models show an important component of asymmetric diapir growth across contrasting base-salt geometries observed in modern, high-resolution 3D-seismic data. Ultimately, results of this study improve our understanding of how pre-salt structures impact salt flow, overburden deformation and distribution of structural styles along rifted passive margins; and work as a guide to the interpretation of complex diapir geometries and their link with pre-salt structures.

References

Abe, S., & Urai, J. L. (2012). Discrete element modeling of boudinage: Insights on rock rheology, matrix flow, and evolution of geometry. *Journal of Geophysical Research*, *117*, B01407. https://doi.org/10.1029/2011JB008555

Albertz, M., & Ings, S. J. (2012). *Some consequences of mechanical stratification in basin-scale numerical models of passive-margin salt tectonics, Geological Society, London, Special Publications*, 363(1), 303–330.

Adam, J., & Krézsek, C. (2012). Basin-scale salt tectonic processes of the Laurentian Basin, eastern Canada: Insights from integrated regional 2D seismic interpretation and 4D physical experiments. *Geological Society, London, Special Publications*, *363*(1), 331–360. https://doi.org/10.1144/SP363.15

Albertz, M., Beaumont, C., Shimeld, J. W., Ings, S. J., & Gradmann, S. (2010). An investigation of salt tectonic structural styles in the Scotian Basin, offshore Atlantic Canada: 1. Comparison of observations with geometrically simple numerical models. *Tectonics*, *29*, TC4017. https://doi.org/10.1029/2009TC002539

Botter, C., Cardozo, N., Hardy, S., Lecomte, I., & Escalona, A. (2014). From mechanical modeling to seismic imaging of faults: A synthetic workflow to study the impact of faults on seismic. *Marine and Petroleum Geology*, *57*, 187–207. https://doi.org/10.1016/j. marpetgeo.2014.05.013

Brun, J. P., & Fort, X. (2011). Salt tectonics at passive margins: Geology versus models. *Marine and Petroleum Geology*, *28*(6), 1123–1145. https://doi.org/10.1016/j.marpetgeo.2011.03.004

Davison, I. (2005). Central Atlantic margin basins of north West Africa: Geology and hydrocarbon potential (Morocco to Guinea). *Journal of African Earth Sciences*, *43*(1-3), 254–274. https://doi.org/10.1016/j.jafrearsci.2005.07.018

Davison, I., Anderson, L., & Nuttall, P. (2012). Salt deposition, loading and gravity drainage in the Campos and Santos salt basins. *Geological Society, London, Special Publications*, *363*(1), 159–174. https://doi.org/10.1144/SP363.8

Deng, C., Gawthorpe, R. L., Finch, E., & Fossen, H. (2017). Influence of a pre-existing basement weakness on normal fault growth during oblique extension: Insights from discrete element modeling. *Journal of Structural Geology*, *105*, 44–61. https://doi.org/10.1016/j.jsg.2017.11.005

Deptuck, M. E., & Kendell, K. L. (2017). A review of Mesozoic-Cenozoic salt tectonics along the Scotian margin, eastern Canada. In J. I. Soto, J. Flinch, & G. Tari (Eds.), *Permo-Triassic Salt Provinces of Europe, North Africa and the Atlantic Margins: Tectonics and Hydrocarbon Potential*, (pp. 287–312). Amsterdam, Netherlands: Elsevier. https://doi.org/10.1016/B978-0-12-809417-4.00014-8

Donzé, F., Mora, P., & Magnier, S. A. (1994). Numerical simulation of faults and shear zones. *Geophysical Journal International*, *116*(1), 46–52. https://doi.org/10.1111/j.1365-246X.1994.tb02126.x

Dooley, T. P., & Hudec, M. R. (2017). The effects of base-salt relief on salt flow and suprasalt deformation patterns—Part 2: Application to the eastern Gulf of Mexico. *Interpretation*, *5*(1), SD25–SD38. https://doi.org/10.1190/INT-2016-0088.1

Dooley, T. P., Hudec, M. R., Carruthers, D., Jackson, M. P., & Luo, G. (2017). The effects of base-salt relief on salt flow and suprasalt deformation patterns—Part 1: Flow across simple steps in the base of salt. *Interpretation*, *5*(1), SD1–SD23. https://doi.org/10.1190/INT-2016-0087.1

Dooley, T. P., Hudec, M. R., & Jackson, M. P. (2012). The structure and evolution of sutures in allochthonous salt. *AAPG Bulletin*, *96*(6), 1045–1070. https://doi.org/10.1306/09231111036

Dooley, T. P., Hudec, M. R., Pichel, L. M., & Jackson, M. P. (2018). *The impact of base-salt relief on salt flow and suprasalt deformation patternsat the autochthonous, paraautochthonous and allochthonous level: insights from physical models*, Geological Society, London, Special Publications, 476, SP476-13.

Dooley, T. P., Jackson, M., & Hudec, M. R. (2007). Initiation and growth of salt-based thrust belts on passive margins: Results from physical models. *Basin Research*, *19*(1), 165–177. https://doi.org/10.1111/j.1365-2117.2007.00317.x

Dooley, T. P., Jackson, M. P., & Hudec, M. R. (2009). Inflation and deflation of deeply buried salt stocks during lateral shortening. *Journal of Structural Geology*, *31*(6), 582–600. https://doi.org/10.1016/j.jsg.2009.03.013

Dooley, T. P., Jackson, M. P. A., & Hudec, M. R. (2015). Breakout of squeezed stocks: Dispersal of roof fragments, source of extrusive salt and interaction with regional thrust faults. *Basin Research*, *27*(1), 3–25. https://doi.org/10.1111/bre.12056

Duffy, O. B., Gawthorpe, R. L., Docherty, M., & Brocklehurst, S. H. (2013). Mobile evaporite controls on the structural style and evolution of rift basins: Danish central graben, North Sea. *Basin Research*, *25*(3), 310–330. https://doi.org/10.1111/bre.12000

Ferrer, O., Jackson, M. P. A., Roca, E., & Rubinat, M. (2012). Evolution of salt structures during extension and inversion of the offshore Parentis Basin (eastern Bay of Biscay). *Geological Society, London, Special Publications*, *363*(1), 361–380. https://doi.org/10.1144/SP363.16

Ferrer, O., McClay, K., & Sellier, N. C. (2017). Influence of fault geometries and mechanical anisotropies on the growth and inversion of hanging-wall synclinal basins: Insights from sandbox models and natural examples. *Geological Society, London, Special Publications*, *439*(1), 487–509. https://doi.org/10.1144/SP439.8

Finch, E., & Gawthorpe, R. (2017). Growth and interaction of normal faults and fault network evolution in rifts: Insights from three-dimensional discrete element modelling. *Geological Society, London, Special Publications*, *439*(1), 219–248. https://doi.org/10.1144/SP439.23

Finch, E., Hardy, S., & Gawthorpe, R. (2003). Discrete element modelling of contractional fault-propagation folding above rigid basement fault blocks. *Journal of Structural Geology*, *25*(4), 515–528. https://doi.org/10.1016/S0191-8141(02)00053-6

Finch, E., Hardy, S., & Gawthorpe, R. (2004). Discrete-element modelling of extensional fault-propagation folding above rigid basement fault blocks. *Basin Research*, *16*(4), 467–488. https://doi.org/10.1111/j.1365-2117.2004.00241.x

Gawthorpe, R. L., & Leeder, M. R. (2000). Tectono-sedimentary evolution of active extensional basins. *Basin Research*, *12*(3–4), 195–218. https://doi.org/10.1111/j.1365-2117.2000.00121.x

Ge, H., Jackson, M. P., & Vendeville, B. C. (1997). Kinematics and dynamics of salt tectonics driven by progradation. *AAPG Bulletin*, *81*(3), 398–423.

Gemmer, L., Beaumont, C., & Ings, S. J. (2005). Dynamic modelling of passive margin salt tectonics: Effects of water loading, sediment properties and sedimentation patterns. *Basin Research*, *17*(3), 383–402. https://doi.org/10.1111/j.1365-2117.2005.00274.x

Gemmer, L., Ings, S. J., Medvedev, S., & Beaumont, C. (2004). Salt tectonics driven by differential sediment loading: Stability analysis and finite-element experiments. *Basin Research*, *16*(2), 199–218. https://doi.org/10.1111/j.1365-2117.2004.00229.x

Gradmann, S., & Beaumont, C. (2016). Numerical modelling study of mechanisms of mid-basin salt canopy evolution and their potential applications to the northwestern Gulf of Mexico. *Basin Research*, *29*(4), 490–520. https://doi.org/10.1111/bre.12186

Gradmann, S., Beaumont, C., & Albertz, M. (2009). Factors controlling the evolution of the Perdido Fold Belt, northwestern Gulf of Mexico, determined from numerical models. *Tectonics*, *28*, TC2002. https://doi.org/10.1029/2008TC002326

Hardy, S., & Finch, E. (2005). Discrete-element modelling of detachment folding. *Basin Research*, *17*(4), 507–520. https://doi.org/10.1111/j.1365-2117.2005.00280.x

Hardy, S., & Finch, E. (2006). Discrete element modelling of the influence of cover strength on basement-involved fault-propagation folding. *Tectonophysics*, *415*(1-4), 225–238. https://doi.org/10.1016/j.tecto.2006.01.002

Hardy, S., & Finch, E. (2007). Mechanical stratigraphy and the transition from trishear to kink-band fault-propagation fold forms above blind basement thrust faults: A discrete-element study. *Marine and Petroleum Geology*, *24*(2), 75–90. https://doi.org/10.1016/j.marpetgeo.2006.09.001

Hudec, M. R., & Jackson, M. P. (2004). Regional restoration across the Kwanza Basin, Angola: Salt tectonics triggered by repeated uplift of a metastable passive margin. *AAPG Bulletin*, *88*(7), 971–990. https://doi.org/10.1306/02050403061

Hudec, M. R., & Jackson, M. P. (2007). Terra infirma: Understanding salt tectonics. *Earth-Science Reviews*, *82*(1-2), 1–28. https://doi.org/10.1016/j.earscirev.2007.01.001

Hudec, M. R., Norton, I. O., Jackson, M. P., & Peel, F. J. (2013). Jurassic evolution of the Gulf of Mexico salt basin. *AAPG Bulletin*, *97*(10), 1683–1710. https://doi.org/10.1306/04011312073

Ings, S. J., & Shimeld, J. W. (2006). A new conceptual model for the structural evolution of a regional salt detachment on the northeast Scotian margin, offshore eastern Canada. *AAPG Bulletin*, *90*(9), 1407–1423. https://doi.org/10.1306/04050605159

Jackson, C. A. L., Jackson, M. P., & Hudec, M. R. (2015). Understanding the kinematics of salt-bearing passive margins: A critical test of competing hypotheses for the origin of the Albian gap, Santos Basin, offshore Brazil. *Geological Society of America Bulletin*, *127*(11–12), 1730–1751. https://doi.org/10.1130/B31290.1

Jackson, C. A. L., Jackson, M. P., Hudec, M. R., & Rodriguez, C. R. (2015). Enigmatic structures within salt walls of the Santos Basin—Part 1: Geometry and kinematics from 3D seismic reflection and well data. *Journal of Structural Geology*, *75*, 135–162. https://doi.org/10.1016/j.jsg.2015.01.010

Jackson, M. P., & Hudec, M. R. (2005). Stratigraphic record of translation down ramps ina passive-margin salt detachment. *Journal of Structural Geology*, *27*(5), 889–911.

Jackson, M. P., & Hudec, M. R. (2017). *Salt Tectonics: Principles and Practice*. UK: Cambridge University Press. https://doi.org/10.1017/9781139003988

Jackson, M. P., Hudec, M. R., Jennette, D. C., & Kilby, R. E. (2008). Evolution of the cretaceous Astrid thrust belt in the ultradeep-water lower Congo Basin, Gabon. *AAPG Bulletin*, *92*(4), 487–511. https://doi.org/10.1306/12030707074

Jackson, M. P. A., & Vendeville, B. C. (1994). Regionalextension as a geologic trigger for diapirism. *Geological Society of America Bulletin*, *106*(1), 57–73.

Johnson, R. B., & DeGraff, J. V. (1988). *Principles of Engineering Geology*. New York: Wiley.

Li, S. Y., & Urai, J. L. (2016). Rheology of rock salt for salt tectonics modeling. *Petroleum Science*, *13*(4), 712–724. https://doi.org/10.1007/s12182-016-0121-6

Liang, W. G., Yang, C. H., Zhao, Y. S., Dusseault, M. B., & Liu, J. (2007). Experimental investigation of mechanical properties of bedded salt rock. *International Journal of Rock Mechanics and Mining Sciences*, *44*(3), 400–411. https://doi.org/10.1016/j.ijrmms.2006.09.007

Mitchell, N. C., Ligi, M., Ferrante, V., Bonatti, E., & Rutter, E. (2010). Submarine salt flows in the central Red Sea. *GSA Bulletin*, *122*(5–6), 701–713. https://doi.org/10.1130/B26518.1

Mohriak, W. U., Macedo, J. M., Castellani, R. T., Rangel, H. D., Barros, A. Z. N., Latgé, M. A. L., et al. (1995). Salt tectonics and structural styles in the deep-water province of the Cabo Frio region, Rio de Janeiro, Brazil. In M. P. A. Jackson, D. G. Roberts, & S. Snelson (Eds.), *Salt tectonics: a global perspective*, AAPG Memoir, (Vol. 65, pp. 273–304).

Mora, P., & Place, D. (1993). A lattice solid model for the nonlinear dynamics of earthquakes. *International Journal of Modern Physics C*, *04*(06), 1059–1074. https://doi.org/10.1306/M65604C13

Mora, P., & Place, D. (1994). Simulation of the frictional stick-slip instability. *Pure and Applied Geophysics*, *143*(1–3), 61–87. https://doi.org/10.1007/BF00874324

Peel, F. J. (2014). The engines of gravity-driven movement on passive margins: Quantifying the relative contribution of spreading vs. gravity sliding mechanisms. *Tectonophysics*, *633*, 126–142. https://doi.org/10.1016/j.tecto.2014.06.023

Peel, F. J., Travis, C. J., & Hossack, J. R. (1995). Genetic structural provinces and salt tectonics of the Cenozoic offshore U.S. Gulf of Mexico: a preliminary analysis. In M. P. A. Jackson, D. G. Roberts, & S. Snelson (Eds.), *Salt tectonics: a global perspective* (pp. 153–175). AAPG Memoir 65.

Pichel, L. M., Finch, E., Huuse, M., & Redfern, J. (2017). The influence of shortening and sedimentation on rejuvenation of salt diapirs: A new discrete-element modelling approach. *Journal of Structural Geology*, *104*, 61–79. https://doi.org/10.1016/j.jsg.2017.09.016

Pichel, L. M., Peel, F., Jackson, C. A.-L., & Huuse, M. (2018). Geometry and kinematics of salt-detached ramp syncline basins. *Journal of Structural Geology*, *115*, 208–230. https://doi.org/10.1016/j.jsg.2018.07.016

Place, D., Lombard, F., Mora, P., & Abe, S. (2002). Simulation of the micro-physics of rocks using LSMearth. In *Earthquake Processes: Physical Modelling, Numerical Simulation and Data Analysis Part I*, (Vol. 159, pp. 1911–1932). Basel, Switzerland: Birkhäuser Basel. https://doi.org/10.1007/s00024-002-8715-x

Quirk, D. G., Schødt, N., Lassen, B., Ings, S. J., Hsu, D., Hirsch, K. K., & Von Nicolai, C. (2012). Salt tectonics on passive margins: Examples from Santos, Campos and kwanza basins. *Geological Society, London, Special Publications*, *363*, 207–244. https://doi.org/10.1144/SP363.10

Rowan, M. G. (2014). Passive-margin salt basins: Hyperextension, evaporite deposition, and salt tectonics. *Basin Research*, *26*(1), 154–182. https://doi.org/10.1111/bre.12043

Rowan, M. G. (2018). *The South Atlantic and Gulf of Mexico salt basins: crustal thinning, subsidence andaccommodation for salt and presalt strata*, *Geological Society, London, Special Publications*, 476, SP476-6.

Rowan, M. G., Peel, F. J., & Vendeville, B. C. (2004). Gravity-driven fold belts on passive margins. In K. R. McKlay (Ed.), *Thrust tectonics and Hydrocarbon Systems*, *AAPG Memoir*, (Vol. 82, pp. 157–182). https://doi.org/10.1306/M82813C9

Rowan, M. G., Trudgill, B. D., & Carl Fiduk, J. (2000). Deep-Water, Salt-Cored Foldbelts: Lessons from the Mississippi Fan and Perdido Foldbelts, Northern Gulf of Mexico. In *Atlantic rifts and continental margins*, *Geophysical Monograph*, (Vol. 115, pp. 173, 173–191, 192). Washington, DC: American Geophysical Union. https://doi.org/10.1029/GM115p0173

Schöpfer, M. P. J., Childs, C., & Walsh, J. J. (2006). Localisation of normal faults in multilayer sequences. *Journal of Structural Geology*, *28*(5), 816–833. https://doi.org/10.1016/j.jsg.2006.02.003

Schultz-Ela, D. D., Jackson, M. P., & Vendeville, B. C. (1993). Mechanics of active salt diapirism. *Tectonophysics*, *228*(3–4), 275–312. https://doi.org/10.1016/0040-1951(93)90345-K

Spiers, C. J., Schutjens, P. M. T. M., Brzesowsky, R. H., Peach, C. J., Liezenberg, J. L., & Zwart, H. J. (1990). Experimental determination of constitutive parameters governing creep of rocksalt by pressure solution. *Geological Society, London, Special Publications*, *54*(1), 215–227. https://doi.org/10.1144/GSL.SP.1990.054.01.21

Tari, G., & Jabour, H. (2013). Salt tectonics along the Atlantic margin of Morocco. *Geological Society, London, Special Publications*, *369*(1), 337–353. https://doi.org/10.1144/SP369.23

Tari, G., Molnar, J., & Ashton, P. (2003). Examples of salt tectonics from West Africa: A comparative approach. *Geological Society, London, Special Publications*, *207*(1), 85–104. https://doi.org/10.1144/GSL.SP.2003.207.5

Tari, G., Molnar, J., Ashton, P., & Hedley, R. (2000). Salt tectonics in the Atlantic margin of Morocco. *The Leading Edge*, *19*(10), 1074–1078. https://doi.org/10.1190/1.1438481

Tari, G., Novotny, B., Jabour, H., & Hafid, M. (2017). Salt tectonics along the Atlantic margin of NW Africa (Morocco and Mauritania). In J. I. Soto, J. Flinch, & G. Tari (Eds.), *Permo-Triassic Salt Provinces of Europe, North Africa and the Atlantic Margins: Tectonics and Hydrocarbon Potential*, (pp. 331–351). Amsterdam, Netherlands: Elsevier. https://doi.org/10.1016/B978-0-12-809417-4.00016-1

Vendeville, B. C., Ge, H., & Jackson, M. P. A. (1995). Scale models of salt tectonics during basement-involved extension. *Petroleum Geoscience*, *1*(2), 179–183.

Vendeville, B. C., & Jackson, M. P. A. (1992). The rise of diapirs during thin-skinned extension. *Marine and Petroleum Geology*, *9*(4), 331–354. https://doi.org/10.1016/0264-8172(92)90047-I

Weijermars, R., Hudec, M. R., Dooley, T. P., & Jackson, M. P. A. (2015). Downbuilding salt stocks and sheets quantified in 3-D analytical models. *Journal of Geophysical Research: Solid Earth*, *120*, 4616–4644. https://doi.org/10.1002/2014JB011704

Weijermars, R., Jackson, M. P. A., & Dooley, T. P. (2014). Quantifying drag on wellbore casings in moving saltsheets. *Geophysical Journal International*, *198*(2), 965–977.

Weijermars, R., Jackson, M. T., & Vendeville, B. (1993). Rheological and tectonic modeling of salt provinces. *Tectonophysics*, *217*(1–2), 143–174. https://doi.org/10.1016/0040-1951(93)90208-2

Weijermars, R., & Schmeling, H. (1986). Scaling of Newtonian and non-Newtonian fluid dynamics without inertia for quantitative modelling of rock flow due to gravity (including the concept of rheological similarity). *Physics of the Earth and Planetary Interiors*, *43*(4), 316–330. https://doi.org/10.1016/0031-9201(86)90021-X